Coupling between viscoelasticity and soft elasticity in main-chain nematic Liquid Crystal Elastomers

L. Rezaei[a], G. Scalet[b], M. Peigney[c], A. Azoug[a,1]

[a]*School of Mechanical & Aerospace Engineering, Oklahoma State University, Stillwater, OK, USA*
[b]*Department of Civil Engineering and Architecture, University of Pavia, Pavia, Italy*
[c]*Laboratoire Navier, Universite Paris-Est, Paris, France*

Abstract

Liquid crystal elastomers (LCEs) are a class of smart elastomers exhibiting unusual mechanical behavior, including large energy dissipation and soft elasticity under uniaxial tensile loading. LCEs are composed of liquid crystal molecules, called mesogens, linked by a network of polymer chains. During deformation, the mesogens orient in the direction of the loading, leading to soft elasticity, which is an increase in strain at constant stress. The combination of mesogen rotation and intrinsic polymer viscoelasticity leads to a nonlinear viscoelastic soft elastic behavior. The aim of this paper is to investigate the coupling between the viscoelastic mechanisms and soft elasticity in main chain LCEs. We propose a rheological model in which the mesogen rotation during deformation is represented by a reversible slider while viscoelastic relaxation mechanisms are modeled as series of Maxwell elements coupled or decoupled with mesogen rotation. Fitting this model to experimental data demonstrate that the coupling between polymer chain viscoelasticity and mesogen rotation is partial, *i.e.* the long-time relaxation mechanisms are coupled and the short-time relaxation mechanisms are decoupled from mesogen rotation. Furthermore, we show that the viscosity of mesogen rotation is not necessary to properly predict the elastic modulus during the soft elasticity but it is needed to properly predict the initiation of the phenomenon.

Keywords: Liquid crystal elastomers, soft elasticity, viscoelasticity, mesogen, polydomain-monodomain transition, constitutive modeling

1. Introduction

Liquid Crystal Elastomers (LCEs) are a class of smart elastomers with unique properties, combining the rubber elasticity of the elastomer network with the anisotropic order of the liquid crystals. Thanks to their unusual reversible shape-memory, optical properties, and biocompatibility, LCEs are advantageous candidates for soft robotics, microfluidics, optics, and bioengineering applications [7, 19, 62, 32, 36].

LCEs are composed of mesogenic molecules or liquid crystals, linked by a network of polymer chains. Mesogens are elongated and relatively rigid molecules that tend to form ordered configurations [10, 57]. Below the glass transition temperature (T_g), LCEs are in the glassy state and the low mobility of the polymer chains prevents any mesogen ordering. Above T_g, LCEs are nematic and the mesogens order naturally in the polydomain state. In this polydomain state, mesogens form micrometer-sized ordered subdomains, each with a unique randomly-oriented director, so that the LCE remains macroscopically isotropic [14]. Stretching a polydomain LCE leads to the orientation of the subdomains in the direction of the applied strain, resulting in monodomain LCE. This phenomenon is denoted as the polydomain-monodomain (PM) transition. Finally, increasing the temperature of the nematic LCE above the nematic-isotropic (NI) transition temperature T_{ni} prevents any ordering of the microstructure. In the isotropic state, mesogens exhibit random directors and

*Corresponding author, Aurelie Azoug, azoug@okstate.edu

LCEs are microscopically and macroscopically isotropic [56]. Each transition involving a change of order is associated to a nonlinear mechanical behavior resulting from the coupling between the orientation of the mesogens with the mechanical deformation of the polymer network: reversible shape-memory actuation during the NI transition and soft elasticity during the PM transition. This paper focuses on the coupling between polymer chain movement and mesogen rotation during soft elasticity at the PM transition.

Soft elasticity is defined as an increase in strain at constant stress [54, 50, 53]. The soft elastic tensile curve is composed of three phases (Fig. 1). First, the material is in the polydomain state and behaves like a classic isotropic polymer network. When the reorientation stress threshold is reached, the polydomain LCE transitions to a monodomain LCE. During this transition, the effective modulus is close to zero and the stress-strain curve exhibits a plateau. Finally, once the microstructure is reoriented in the direction of the stretch, the LCE is in the monodomain phase, and further stretching results in stretching the polymer network, which exhibits the usual hyperelastic behavior, although the mechanical behavior is now highly anisotropic.

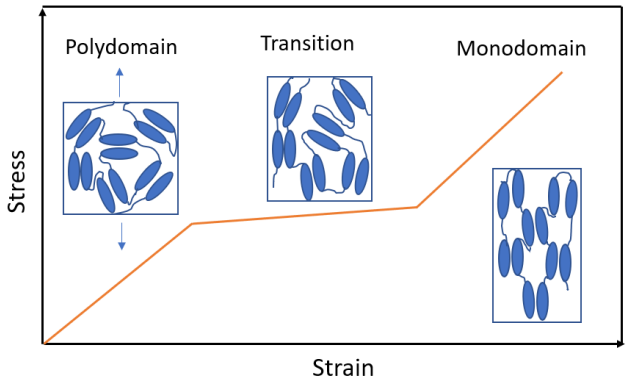

Figure 1: Mesogen orientation and mechanical behavior of LCEs in polydomain, PM transition, and monodomain phases. Soft elasticity corresponds to the PM transition region.

The soft elasticity behavior of LCEs arises from the cooperative alignment and rotation of the elongated mesogens in the direction of applied strain. This enables large deformation with minimal energy input and is characterized by a plateau region in the stress-strain curve [54, 50, 53]. This unique response is due to the anisotropy of the liquid crystalline phase and the coupling between mesogen orientation and polymer chain deformation [34, 54, 14]. Although an ideal soft elasticity leads to a perfect plateau of zero modulus, non ideal loading conditions, such as an increased strain rate, lead to a soft elastic region with a low but non-zero modulus (Fig. 1) [4] Although the physical origin of soft elasticity as resulting from the coupling between mesogen and polymer chains, understanding this coupling and the accompanying time-dependent effects and integrating it in constitutive models remains challenging.

Multiple molecular and macroscopic models have been proposed to study and predict the mechanical behavior of LCEs. At the molecular scale, the material cannot be modeled as a continuum medium and methods such as Monte Carlo (MC) algorithms and molecular dynamics (MD) are commonly used to investigate molecular interactions and deformation mechanisms. Thus, molecular models can elucidate the molecular origin of the highly-nonlinear macroscopic properties of LCEs [63, 40, 30, 39, 26]. For example, researchers showed that the soft elasticity of LCEs results from the coupling between mesogen orientation and position in the polymer network using an MC model [30] and occurs through cluster rotation and domain growth using MD simulations [60]. MD is also an efficient method to investigate the movement of molecules during actuation [47, 31, 20]. MC algorithms are limited to simulations under thermodynamic equilibrium conditions, while MD methods are adequate for time-dependent and equilibrium problems [60]. However, the computational cost of MD methods is high, making them unsuitable for large-scale simulations.

Different approaches have been reported to predict soft elasticity in hyperelastic constitutive laws. A

general constitutive model of ideal monodomain nematic solids [57] used a neoclassical strain-energy function [55, 58, 6] and reliably models the soft elastic behavior of LCEs in the nematic domain [11]. A coarse-grain development of this strain energy function provided a robust simulation of soft elasticity including the local director reorientation [9]. The neoclassical framework has also been combined with the pseudo-elastic theory for particle reinforced rubber [28, 12] to formulate a phenomenological pseudo-energy function of nematic LCEs, which better predicts the soft elastic behavior [25]. Slightly departing from these strategies, a phase-field approach considered microscopic liquid crystal forces combined with a simplified Landau and distortional energy functions and predicted the soft elasticity and the stripe domains in the microstructure [27].

In combination with soft elasticity, LCEs also exhibit viscoelasticity [45, 16, 15, 29, 8, 18, 17, 4]. To identify time-dependent deformation mechanisms, Azoug et al. [4] studied the rate-dependent behavior of a nematic LCE from the polydomain to the monodomain state and back over a large range of strain rates and temperatures. Three relaxation mechanisms were detected: (i) spectrum of relaxation mechanisms associated to the usual behavior of the polymer network, (ii) short-time relaxation mechanisms connected to changes in director orientation in nematic domains, and (iii) a slow relaxation mechanism related to the relaxation of the polydomain texture and cooperative motions [18, 51, 4]. A fourth small-scale mechanism corresponding to the rotation of a mesogen on the polymer chain is discussed in the literature [35]. However, measurements of mesogen rotation in liquid crystal polymers, *i.e.* non-crosslinked polymers, have shown that the relaxation associated with this mechanisms is two orders of magnitude faster than the relaxation of a cross-linked polymer network and, hence, insignificant in LCEs [35]. This does not imply that mesogen reorientation has no impact on the time-dependent behavior of the LCE. On the contrary, mechanisms associated with the director reorientation in nematic domains, measured for example in polydomain side-chain LCEs [51] or smectic LCEs [1], are still related to mesogen rotation but involve friction with the neighboring polymer chains because of their larger scale.

The time-dependent behavior of liquid crystal fluids has been modeled in the continuum mechanics framework through the dissipation principle, considering them dissipative ordered fluids [22, 42, 43]. The models combine a Rayleigh dissipative function in the Leslie-Ericksen form with a free energy function containing an elastic and a liquid crystal contribution. This modeling approach was then extended to the behavior of LCEs under small strain and small director rotation, differentiating the dissipations originating from mesogen rotation from the energy dissipated by the polymer network [49]. Finally, the behavior of LCEs in large strain and large director rotation was predicted following the same modeling approach [65, 64, 52]. As pointed out by Wang et al. [52], the Rayleigh dissipation function in the Leslie-Ericksen form [49, 65, 64] explicitly depends on the rate of strain tensor, implying that the model does not have an instantaneous stress response. The model developed in [52] is limited to monodomain LCEs, *i.e.* LCEs with a uniform director field. Consequently, it is assumed that the order parameter remains constant and the model is not able to reproduce the behavior of a randomly-oriented polydomain LCE or the PM transition. Notably, Wang et al. [52] hypothesized that the viscous deformation mechanisms associated with the mesogen rotation are independent from the viscosity associated with the polymer network.

The goal of this paper is to address the three following questions regarding the viscoelastic relaxation mechanisms attributed to the polymer chains and to the mesogens: *(1) How is mesogen rotation coupled with polymer viscoelasticity?*, *(2) Is the mechanism of mesogen rotation viscous?*, and *(3) Is the initiation of mesogen rotation viscous?*.

The soft elasticity phenomenon is similar to the superelasticity behavior observed in shape-memory alloys (SMAs), which originates from the phase transition between martensite and austenite [46]. In both cases, a large increase in strain at constant stress is observed as a result of a phase transition. Although the transition mechanisms in SMAs result from changes in atomic order rather than molecular rearrangements, the macroscopic behavior is qualitatively similar and is well represented by the so-called Souza-Auricchio model [3, 44, 33]. Taking inspiration from superelasticity models, we propose a phenomenological model of LCEs where an internal variable, the transformation strain, controls the PM transition and the soft elasticity. The model is expanded to time-dependent behavior through strategically placed Maxwell elements. The proposed model is phenomenological and as such, is not limited to monodomain LCEs. Thus, it can predict the soft elasticity arising during the PM transition. The mechanism of mesogen rotation is modeled as

elastic, *i.e.* non-dissipative, but can be coupled to the polymer network viscoelasticity. This time-dependent model then provides a tool to investigate the coupling between viscoelastic relaxation mechanisms and soft elasticity in LCEs. Since modeling actuation is not an objective of the current model, the model is not concerned with variations in temperature.

The paper is organized as follows. In Section 2, we introduce the proposed rheological model and discuss the development of the constitutive equations. This includes an examination of three different distributions for the viscoelastic relaxation mechanisms. In Section 3, we wish to address the discussion questions by comparing our model with experimental data. Finally, conclusions are given in Section 4.

2. Model

The generalized plasticity model [13, 23], which efficiently models inelastic behavior, has been successfully adapted to the superelastic behavior of SMAs by including a sliding device between the two phases, martensite and austenite [24, 3, 44]. Here, we extend the approach to develop a small strain model, where the sliding device transitions between a polydomain and monodomain orientation in LCEs.

2.1. Strain decomposition

The total strain tensor $\boldsymbol{\varepsilon}$ is the control variable, additively decomposed into a volumetric tensor $\boldsymbol{\varepsilon}^{vol}$ (equ. (1)) and a deviatoric strain tensor $\boldsymbol{e}$ (equ. (2)):

$$\boldsymbol{\varepsilon}^{vol} = \frac{1}{3}\theta\mathbf{1} \tag{1}$$

$$\boldsymbol{e} = \boldsymbol{\varepsilon} - \boldsymbol{\varepsilon}^{vol} \tag{2}$$

where θ is $tr(\boldsymbol{\varepsilon})$ and $\mathbf{1}$ is the unit tensor. The behavior is assumed isochoric. In addition, we assume the volumetric behavior entirely linear elastic. The viscoelasticity and nonlinearity resulting from mesogen reorientation are assumed deviatoric based on experimental evidence [59].

2.2. Rheological model and Helmholtz free energy

We propose a rheological model for the deviatoric part of nematic LCEs where (i) a single spring with shear modulus G^{tr} represents the elastic response of the material, (ii) a sliding device represents the PM transition, where the device slides at a certain stress threshold with zero friction, (iii) A series of M coupled Maxwell elements, each composed of a spring with shear modulus G_k^{tr} and a dashpot with viscosity η_k^* ($k = 1, ..., M$), represent the coupled viscoelastic relaxation mechanisms, and finally (iv) a series of N decoupled elements, each consisting of spring with shear modulus G_k and a dashpot with viscosity η_k ($k = 1, ..., N$), represent the decoupled viscoelastic relaxation mechanisms (Fig. 2).

Figure 2: Proposed rheological model

The deviatoric transformation strain $\boldsymbol{e}^{tr}$ is an internal variable introduced to quantify the strain-induced movement of the sliding device and represents the transformation of the LCE from polydomain to monodomain. $\boldsymbol{e}^{tr}$ satisfies the saturation constraint $\|\boldsymbol{e}^{tr}\| \leq \varepsilon_L$, where ε_L is the maximum residual strain and $\|.\|$ indicates the Euclidean norm.

The deviatoric strain tensor $\boldsymbol{e}^*$ in the coupled Maxwell element k consists of the elastic strain $\boldsymbol{e}_k^{*e}$ in the spring and the viscoelastic strain $\boldsymbol{e}_k^{*v}$ in the dashpot, *i.e.* $\boldsymbol{e}^* = \boldsymbol{e}_k^{*e} + \boldsymbol{e}_k^{*v}$, $k = 1, ..., M$. Similarly, in the decoupled Maxwell element k, the deviatoric strain is divided in elastic $\boldsymbol{e}_k^e$ and viscoelastic $\boldsymbol{e}_k^v$ strains, *i.e.* $\boldsymbol{e} = \boldsymbol{e}_k^e + \boldsymbol{e}_k^v$, $k = 1, ..., N$. The viscoelastic strains $\boldsymbol{e}_k^{*v}$ and $\boldsymbol{e}_k^v$ are internal variables of the model.

The Helmholtz free energy of the material Φ is decomposed into the volumetric Ψ^{vol}, transition Ψ^{tr}, coupled elastic Ψ^e, coupled viscoelastic Ψ_k^{*v}, and decoupled viscoelastic Ψ_k^v components,

$$\Phi(\theta, \boldsymbol{e}, \boldsymbol{e}^{tr}, \boldsymbol{e}_k^{*v}, \boldsymbol{e}_k^v) = \Psi^{vol}(\theta) + \Psi^{tr}(\boldsymbol{e}^{tr}) + \Psi^e(\boldsymbol{e}, \boldsymbol{e}^{tr}) + \sum_{k=1}^{M} \Psi_k^{*v}(\boldsymbol{e}, \boldsymbol{e}^{tr}, \boldsymbol{e}_k^{*v}) + \sum_{k=1}^{N} \Psi_k^v(\boldsymbol{e}, \boldsymbol{e}_k^v) \tag{3}$$

where $\Psi^{vol}(\theta) = \frac{1}{2}\kappa\theta^2$ characterizes the entire volumetric response, with κ the bulk modulus. The transition is defined by

$$\Psi^{tr} = \tau_M \|\boldsymbol{e}^{tr}\| + \frac{1}{2} h \|\boldsymbol{e}^{tr}\|^2 + \jmath_{\varepsilon_L}(\boldsymbol{e}^{tr}) \tag{4}$$

where the critical stress τ_M determines the onset of the transition, h defines the possible hardening during the transition, and the function $\jmath_{\varepsilon L}(\boldsymbol{e}^{tr})$ is used to satisfy the saturation constraint, $\|\boldsymbol{e}^{tr}\| \leq \varepsilon_L$ according to

$$\jmath_{\varepsilon_L}(\boldsymbol{e}^{tr}) = \begin{cases} 0 & \text{if } \|\boldsymbol{e}^{tr}\| \leq \varepsilon_L \\ +\infty & \text{otherwise} \end{cases} \tag{5}$$

The remaining elastic and viscoelastic components of the free energy are defined as

$$\Psi^{e} = G^{tr} \|\boldsymbol{e} - \boldsymbol{e}^{tr}\|^2 \tag{6}$$

$$\Psi_k^{*v} = G_k^{*tr} \|\boldsymbol{e} - \boldsymbol{e}_k^{*v} - \boldsymbol{e}^{tr}\|^2 \tag{7}$$

$$\Psi_k^{v} = G_k \|\boldsymbol{e} - \boldsymbol{e}_k^{v}\|^2 \tag{8}$$

where G denotes a generic shear modulus and the superscript tr indicates a dependence on the transition strain $\boldsymbol{e}^{tr}$. Experimental measurements show that the LCE apparent modulus varies between the polydomain and monodomain phases[4]. Consequently, we assume the modulus of the coupled elastic element G^{tr} is affected by mesogen rotation and continuously evolving during the transition from a polydomain modulus G_p at $\boldsymbol{e}^{tr} = \boldsymbol{0}$ to a monodomain modulus G_m at $\|\boldsymbol{e}^{tr}\| = \varepsilon_L$. Similarly, the moduli of the coupled viscoelastic elements G_k^{*tr} are evolving from G_{kp}^{*} in the polydomain to G_{km}^{*} in the monodomain. The shear moduli associated with decoupled Maxwell elements G_k are constant through the transition.

Following Auricchio et al. [2], we adopt the expressions (9) for the shear moduli of the elastic G^{tr} and coupled viscoelastic elements G_k^{*tr} continuously evolving with $\boldsymbol{e}^{tr}$ from a polydomain value $(\bullet)_p$ to a monodomain value $(\bullet)_m$ with $(\bullet)_p > (\bullet)_m$. This expressions ensure that $\frac{\partial \sigma}{\partial \varepsilon} \approx 0$ for $h = 0$.

$$G^{tr}(\boldsymbol{e}^{tr}) = \frac{\varepsilon_L}{\frac{\varepsilon_L - \|\boldsymbol{e}^{tr}\|}{G_p} + \frac{\|\boldsymbol{e}^{tr}\|}{G_m}}, \qquad G_k^{*tr}(\boldsymbol{e}^{tr}) = \frac{\varepsilon_L}{\frac{\varepsilon_L - \|\boldsymbol{e}^{tr}\|}{G_{kp}^{*}} + \frac{\|\boldsymbol{e}^{tr}\|}{G_{km}^{*}}} \tag{9}$$

2.3. Constitutive equations

The constitutive equations for the volumetric p and deviatoric $\boldsymbol{s}$ part of the stress tensor $\boldsymbol{\sigma}$ are expressed as

$$p = \frac{\partial \Phi}{\partial \theta} = \kappa\theta \tag{10}$$

$$\begin{aligned} \boldsymbol{s} &= \frac{\partial \Phi}{\partial \boldsymbol{e}} = \boldsymbol{s}^{e} + \sum_{k=1}^{N} \boldsymbol{s}_k^{v} + \sum_{k=1}^{M} \boldsymbol{s}_k^{*v} \\ &= 2G^{tr}\left(\boldsymbol{e} - \boldsymbol{e}^{tr}\right) + 2\sum_{k=1}^{N} G_k\left(\boldsymbol{e} - \boldsymbol{e}_k^{v}\right) + 2\sum_{k=1}^{M} G_k^{*tr}\left(\boldsymbol{e} - \boldsymbol{e}^{tr} - \boldsymbol{e}_k^{*v}\right) \end{aligned} \tag{11}$$

As the derivatives of the elastic G^{tr} and viscoelastic G_k^{*tr} shear moduli with respect to $\boldsymbol{e}^{tr}$ are $\partial G^{tr}/\partial \boldsymbol{e}^{tr} = L/{K^{tr}}^2$ and $\partial G_k^{*tr}/\partial \boldsymbol{e}^{tr} = L_k^{*}/{K_k^{*tr}}^2$, the thermodynamic stress-like quantity $\boldsymbol{\chi} = -\frac{\partial \Phi}{\partial \boldsymbol{e}^{tr}}$ associated with $\boldsymbol{e}^{tr}$ is expressed as

$$\boldsymbol{\chi} = G_0^{*tr}\left(\boldsymbol{e} - \boldsymbol{e}^{tr}\right) - \sum_{k=1}^{M} 2G_k^{*tr}\boldsymbol{e}_k^{*v} - \left(d + h\|\boldsymbol{e}^{tr}\| + \tau_M + \gamma\right)\partial\|\boldsymbol{e}^{tr}\| \tag{12}$$

where

$$G_0^{*tr} = 2\left(G^{tr} + \sum_{k=1}^{M} G_k^{*tr}\right) \tag{13}$$

$$d = \frac{L}{K^{tr2}}\|\boldsymbol{e} - \boldsymbol{e}^{tr}\|^2 + \sum_{k=1}^{M} \frac{L_k^*}{K_k^{*tr2}}\|\boldsymbol{e} - \boldsymbol{e}^{tr} - \boldsymbol{e}_k^{*v}\|^2 \tag{14}$$

$$L = \varepsilon_L G_m G_p (G_m - G_p) \qquad L_k^* = \varepsilon_L G_{km}^* G_{kp}^* (G_{km}^* - G_{kp}^*) \tag{15}$$

$$K^{tr} = G_m(\varepsilon_L - \|\boldsymbol{e}^{tr}\|) + G_p\|\boldsymbol{e}^{tr}\| \qquad K_k^{*tr} = G_{km}^*(\varepsilon_L - \|\boldsymbol{e}^{tr}\|) + G_{kp}^*\|\boldsymbol{e}^{tr}\| \tag{16}$$

and $\partial \jmath_{\varepsilon_L}(\boldsymbol{e}^{tr}) = \gamma \frac{\boldsymbol{e}^{tr}}{\|\boldsymbol{e}^{tr}\|}$ with

$$\gamma = \begin{cases} 0 & \text{if } \|\boldsymbol{e}^{tr}\| < \varepsilon_L \\ \geq 0 & \text{if } \|\boldsymbol{e}^{tr}\| = \varepsilon_L \end{cases} \tag{17}$$

The quantity $\partial\|\boldsymbol{e}^{tr}\|$ is not single-valued when $\boldsymbol{e}^{tr} = \boldsymbol{0}$. According to [5],

$$\partial\|\boldsymbol{e}^{tr}\| = \begin{cases} \boldsymbol{e}^{tr}/\|\boldsymbol{e}^{tr}\| & \text{if } \boldsymbol{e}^{tr} \neq \boldsymbol{0} \\ \{\boldsymbol{\tau} : tr\boldsymbol{\tau} = 0, \|\boldsymbol{\tau}\| \leq 1\} & \text{if } \boldsymbol{e}^{tr} = \boldsymbol{0} \end{cases} \tag{18}$$

2.3.1. Evolution equation of $\boldsymbol{e}^{tr}$

The model can introduce a hysteresis around the transition through the Mises-type limit function $F(\boldsymbol{\chi})$ (equ.(19))

$$F(\boldsymbol{\chi}) = \|\boldsymbol{\chi}\| - R_y \tag{19}$$

where R_y is the radius of the elastic domain during transition around critical stress that controls the width of the hysteresis. The evolution equation for the internal variable $\boldsymbol{e}^{tr}$ is then:

$$\dot{\boldsymbol{e}}^{tr} = \dot{\lambda}\frac{\partial F}{\partial \boldsymbol{\chi}} = \dot{\lambda}\partial\|\boldsymbol{\chi}\| \tag{20}$$

where $\dot{\lambda}$ is the non-negative consistency parameter and $\partial\|\boldsymbol{\chi}\|$ is given as:

$$\partial\|\boldsymbol{\chi}\| = \begin{cases} \boldsymbol{\chi}/\|\boldsymbol{\chi}\| & \text{if } \boldsymbol{\chi} \neq \boldsymbol{0} \\ \{\boldsymbol{\tau} : tr\boldsymbol{\tau} = 0 \ , \ \|\boldsymbol{\tau}\| \ \leq 1\} & \text{if } \boldsymbol{\chi} = \boldsymbol{0} \end{cases} \tag{21}$$

Similarly to the plasticity consistency conditions, the classical Kuhn-Tucker conditions $\dot{\lambda} \geq 0$, $F \leq 0$, $\dot{\lambda}F = 0$ complete the evolution equation, with the transition strain evolving in the slider rather than plastic flow in a classical plasticity model [38, 37]. The Kuhn-Tucker conditions express that, during the transition, $\dot{\lambda} \neq 0$ and $\boldsymbol{e}^{tr}$ is changing while $F(\boldsymbol{\chi}) = 0$ and $\|\boldsymbol{\chi}\| = R_y$. Outside of the transition, $\dot{\lambda} = 0$ and $\boldsymbol{e}^{tr}$ is constant while $0 \leq \|\boldsymbol{\chi}\| < R_y$.

Following the time discretization and incremental energy minimization scheme described in detail in [33], the updated value of $\boldsymbol{e}^{tr}$ needs to satisfy the stationary equation (equ.(22)).

$$\begin{aligned} 0 &= -\boldsymbol{\chi} + R_y\partial\|\boldsymbol{e}^{tr} - \boldsymbol{e}_n^{tr}\| \\ &= G_0^{*tr}\left(\boldsymbol{e}^{tr} - \boldsymbol{e}\right) + \sum_{k=1}^{M} 2G_k^{*tr}\boldsymbol{e}_k^{*v} + \left(d + h\|\boldsymbol{e}^{tr}\| + \tau_M + \gamma\right)\partial\|\boldsymbol{e}^{tr}\| + R_y\partial\|\boldsymbol{e}^{tr} - \boldsymbol{e}_n^{tr}\| \end{aligned} \tag{22}$$

where all quantities are expressed at time step t_{n+1} except $\boldsymbol{e}_n^{tr}$ expressed at time t_n, and

$$\partial\|\boldsymbol{e}^{tr} - \boldsymbol{e}_n^{tr}\| = \begin{cases} \frac{\boldsymbol{e}^{tr} - \boldsymbol{e}_n^{tr}}{\|\boldsymbol{e}^{tr} - \boldsymbol{e}_n^{tr}\|} & \text{if } \boldsymbol{e}^{tr} \neq \boldsymbol{e}_n^{tr} \\ \{\boldsymbol{\tau} : tr\boldsymbol{\tau} = 0, \|\boldsymbol{\tau}\| \leq 1\} & \text{if } \boldsymbol{e}^{tr} = \boldsymbol{e}_n^{tr} \end{cases} \tag{23}$$

There are three phases in the evolution of $\boldsymbol{e}^{tr}$. In the polydomain phase, there is no transition, *i.e.* $\boldsymbol{e}^{tr} = \mathbf{0}$. During the transition, $\boldsymbol{e}^{tr}$ increases up to ε_L. Finally, in the monodomain phase, the transition strain is constant, *i.e.* $\|\boldsymbol{e}^{tr}\| = \varepsilon_L$. Accordingly:

- Polydomain phase or elastic evolution, $\|\boldsymbol{e}^{tr}\| \leq \varepsilon_L$ and $\gamma = 0$.
  If $\boldsymbol{e}_n^{tr} = \mathbf{0}$, as the evolution is elastic in this case, $\boldsymbol{e}^{tr} = \mathbf{0}$ and $\partial\|\boldsymbol{e}^{tr} - \boldsymbol{e}_n^{tr}\| = \boldsymbol{\tau}$, leading to

$$G_0^{*tr}\boldsymbol{e} - \sum_{k=1}^{M} 2G_k^{*tr}\boldsymbol{e}_k^{*v} = (\tau_M + R_y + d_0)\,\boldsymbol{\tau} \tag{24}$$

  where

$$d_0 = d\Big|_{\boldsymbol{e}^{tr}=\mathbf{0}} = \frac{L}{G_m^2\varepsilon_L^2}\|\boldsymbol{e}\|^2 + \sum_{k=1}^{M}\frac{L_k^*}{G_{km}^{*2}\varepsilon_L^2}\|\boldsymbol{e} - \boldsymbol{e}_k^{*v}\|^2 \tag{25}$$

  Taking the norm on both sides on this expression gives $\boldsymbol{e}^{tr} = \mathbf{0}$ if and only if

$$\left\| G_0^{*tr}\boldsymbol{e} - \sum_{k=1}^{M} 2G_k^{*tr}\boldsymbol{e}_k^{*v} \right\| \leq \tau_M + R_y + d_0 \tag{26}$$

  If $\boldsymbol{e}_n^{tr} \neq \mathbf{0}$, two cases arise. First, if $\boldsymbol{e}^{tr} = \boldsymbol{e}_n^{tr}$, there is no additional transition, $\partial\|\boldsymbol{e}^{tr} - \boldsymbol{e}_n^{tr}\| = \boldsymbol{\tau}$ and

$$\left\| G_0^{*tr}(\boldsymbol{e} - \boldsymbol{e}_n^{tr}) - (\tau_M + d_n)\frac{\boldsymbol{e}_n^{tr}}{\|\boldsymbol{e}_n^{tr}\|} - h\boldsymbol{e}_n^{tr} - \sum_{k=1}^{M} 2G_k\boldsymbol{e}_k^{v} \right\| \leq R_y \tag{27}$$

  where

$$d_n = d\Big|_{\boldsymbol{e}^{tr}=\boldsymbol{e}_n^{tr}} = \frac{L}{K^{tr^2}}\|\boldsymbol{e} - \boldsymbol{e}_n^{tr}\|^2 + \sum_{k=1}^{M}\frac{L_k^*}{K_k^{*tr^2}}\|\boldsymbol{e} - \boldsymbol{e}_k^{*v} - \boldsymbol{e}_n^{tr}\|^2 \tag{28}$$

  Second, if $\boldsymbol{e}^{tr} = \mathbf{0}$ and $\partial\|\boldsymbol{e}^{tr}\| = \boldsymbol{\tau}$, the expression becomes

$$\left\| G_0^{*tr}\boldsymbol{e} - \sum_{k=1}^{M} 2G_k^{*tr}\boldsymbol{e}_k^{*v} + R_y\frac{\boldsymbol{e}_n^{tr}}{\|\boldsymbol{e}_n^{tr}\|} \right\| \leq \tau_M + d_0 \tag{29}$$

$$\tag{30}$$

- PM transition $\boldsymbol{e}^{tr} \neq \{\mathbf{0}, \boldsymbol{e}_n^{tr}\}$, $\|\boldsymbol{e}^{tr}\| < \varepsilon_L$ and $\gamma = 0$. These conditions directly lead to

$$\|\boldsymbol{e}^{tr} - \boldsymbol{e}_n^{tr}\| = \frac{\|\boldsymbol{b}\| - R_y}{f} \tag{31}$$

  where

$$\boldsymbol{b} = G_0^{*tr}\boldsymbol{e} - \sum_{k=1}^{M} 2G_k^{*tr}\boldsymbol{e}_k^{*v} - f\boldsymbol{e}_n^{tr} \tag{32}$$

$$f = G_0^{*tr} + h + \frac{d + \tau_M}{\|\boldsymbol{e}^{tr}\|} \tag{33}$$

$$d = \frac{L}{K^{tr^2}}\|\boldsymbol{e} - \boldsymbol{e}^{tr}\|^2 + \sum_{k=1}^{M}\frac{L_k^*}{K_k^{*tr^2}}\|\boldsymbol{e} - \boldsymbol{e}_k^{*v} - \boldsymbol{e}^{tr}\|^2 \tag{34}$$

  and finally, we obtain

$$\boldsymbol{e}^{tr} = \frac{1}{f}\left(G_0^{*tr}\boldsymbol{e} - \sum_{k=1}^{M} 2G_k^{*tr}\boldsymbol{e}_k^{*v} - R_y\frac{\boldsymbol{b}}{\|\boldsymbol{b}\|} \right) \tag{35}$$

- Monodomain: When the polydomain phase has totally transformed into a monodomain phase, $\|\boldsymbol{e}^{tr}\| = \varepsilon_L$, $\gamma \neq 0$, $G^{tr} = G_m$, $G_k^{*tr} = G_{km}^*$, $G_0^{*tr} = G_{0m}^* = 2\left(G_m + \sum_{k=1}^M G_{km}^*\right)$, $K^{tr} = G_p\varepsilon_L$, and $K_k^{*tr} = G_{kp}^*\varepsilon_L$. Writing $\|\boldsymbol{e}^{tr} - \boldsymbol{e}_n^{tr}\|$ as

$$\begin{aligned}
\|\boldsymbol{e}^{tr} - \boldsymbol{e}_n^{tr}\| &= \frac{\|\boldsymbol{b}'\| - R_y}{f'} && (36)\\
\boldsymbol{b}' &= G_{0m}^*\boldsymbol{e} - \sum_{k=1}^M 2G_{km}^*\boldsymbol{e}_k^{*v} - f'\boldsymbol{e}_n^{tr} && (37)\\
f' &= G_{0m}^* + h + \frac{d' + \tau_M + \gamma}{\varepsilon_L} && (38)\\
d' &= \frac{L}{G_p^2\varepsilon_L^2}\|\boldsymbol{e} - \boldsymbol{e}^{tr}\|^2 + \sum_{k=1}^M \frac{L_k^*}{G_{kp}^{*2}\varepsilon_L^2}\|\boldsymbol{e} - \boldsymbol{e}_k^{*v} - \boldsymbol{e}^{tr}\|^2 && (39)
\end{aligned}$$

leads to

$$\boldsymbol{e}^{tr} = \frac{1}{f'}\left(G_{0m}^*\boldsymbol{e} - \sum_{k=1}^M 2G_{km}^*\boldsymbol{e}_k^{*v} - R_y\frac{\boldsymbol{b}'}{\|\boldsymbol{b}'\|}\right) \quad (40)$$

Finally, using $\|\boldsymbol{e}^{tr}\| = \varepsilon_L$, we develop an expression for γ,

$$\gamma = \left\|G_{0m}^*\boldsymbol{e} - \sum_{k=1}^M 2G_{km}^*\boldsymbol{e}_k^{*v} - R_y\frac{\boldsymbol{b}'}{\|\boldsymbol{b}'\|}\right\| - \tau_M - d' - (G_{0m}^* + h)\varepsilon_L \quad (41)$$

2.3.2. Evolution equation of $\boldsymbol{e}_k^{*v}$

Since the stress $\boldsymbol{s}_k^{*v}$ in the coupled viscoelastic element k is $\boldsymbol{s}_k^{*v} = \frac{\partial\Psi_k^{*v}}{\partial\boldsymbol{e}} = 2G_k^{*tr}(\boldsymbol{e} - \boldsymbol{e}_k^{*v} - \boldsymbol{e}^{tr})$ (equ. (11)) and the stress in the damper in the same element is $\boldsymbol{s}_k^{*v} = \eta_k\dot{\boldsymbol{e}}_k^{*v}$, the evolution equation for the internal variable $\boldsymbol{e}_k^{*v}$ is expressed as:

$$\dot{\boldsymbol{e}}_k^{*v} = \frac{1}{\tau_k^*}(\boldsymbol{e} - \boldsymbol{e}_k^{*v} - \boldsymbol{e}^{tr}) \quad (42)$$

where $\tau_k^* = \eta_k/2G_k^{*tr}$. We can solve equation (42) with the initial conditions (43).

$$\begin{cases}\boldsymbol{e}_k^{*v}(0) = \boldsymbol{0}\\ \lim_{t\to\infty}\boldsymbol{e}_k^{*v} = \boldsymbol{0}\end{cases} \quad (43)$$

Classically, we multiply equation (42) by e^{t/τ_k}, integrate it from 0 to time t, and obtain

$$\boldsymbol{e}_k^{*v}(t) = \int_0^t \frac{1}{\tau_k^*}e^{(\xi-t)/\tau_k^*}(\boldsymbol{e} - \boldsymbol{e}^{tr})\,d\xi = \boldsymbol{e} - \boldsymbol{e}^{tr} - \boldsymbol{h}_k^*(t) \quad (44)$$

where

$$\boldsymbol{h}_k^*(t) = \int_0^t e^{(\xi-t)/\tau_k^*}(\dot{\boldsymbol{e}} - \dot{\boldsymbol{e}}^{tr})\,d\xi \quad (45)$$

In a discrete time framework, $\boldsymbol{h}_k^{*n+1}$ at time t_{n+1} can be found from the known $\boldsymbol{h}_k^{*n}$ at time t_n as:

$$\begin{aligned}
\boldsymbol{h}_k^{*n+1} &= e^{(t_n - t_{n+1})/\tau_k^*}\boldsymbol{h}_k^{*n} + e^{(t_n - t_{n+1})/2\tau_k^*}(\boldsymbol{e}_{n+1} - \boldsymbol{e}_{n+1}^{tr} - \boldsymbol{e}_n + \boldsymbol{e}_n^{tr}) && (46)\\
& && (47)
\end{aligned}$$

2.3.3. Evolution equation of $\boldsymbol{e}_k^v$

The stress $\boldsymbol{s}_k^v$ in the decoupled viscoelastic element k is $\boldsymbol{s}_k^v = \frac{\partial \Psi_k^v}{\partial \boldsymbol{e}} = 2G_k(\boldsymbol{e} - \boldsymbol{e}_k^v)$ (equ. (11)) and the evolution equation of $\boldsymbol{e}_k^v$ is obtained as

$$\dot{\boldsymbol{e}}_k^v = \frac{1}{\tau_k}(\boldsymbol{e} - \boldsymbol{e}_k^v) \tag{48}$$

where $\tau_k = \eta_k/2G_k$. Considering the initial condition (49),

$$\begin{cases} \boldsymbol{e}_k^v(0) = \boldsymbol{0} \\ \lim_{t\to\infty} \boldsymbol{e}_k^v = \boldsymbol{0} \end{cases} \tag{49}$$

the internal variable $\boldsymbol{e}_k^v$ is explicitly expressed as:

$$\boldsymbol{e}_k^v(t) = \int_0^t \frac{1}{\tau_k} e^{(\xi - t)/\tau_k} \boldsymbol{e}\, d\xi = \boldsymbol{e} - \boldsymbol{h}_k(t) \tag{50}$$

where

$$\boldsymbol{h}_k(t) = \int_0^t e^{(\xi - t)/\tau_k} \dot{\boldsymbol{e}}\, d\xi \tag{51}$$

In a discrete time framework, $\boldsymbol{h}_k^{n+1}$ can be found as:

$$\boldsymbol{h}_k^{n+1} \quad = \quad e^{(t_n - t_{n+1})/\tau_k} \boldsymbol{h}_k^n + e^{(t_n - t_{n+1})/2\tau_k} (\boldsymbol{e}_{n+1} - \boldsymbol{e}_n) \tag{52}$$

where $\boldsymbol{h}_k^n$ is known from time t_n.

2.3.4. Discrete problem

PM transition. The system of equations (53)-(57) is solved at each time t_{n+1} during the transition to determine the values of the internal variables $\boldsymbol{e}_{n+1}^{tr}$ and $\boldsymbol{e}_{k,n+1}^{*v}$, using a Newton-Raphson method. The stiffness matrix used for this resolution is presented in Appendix A.

$$(H_1) \qquad x - \|\boldsymbol{e}^{tr}\| = 0 \tag{53}$$

$$\left(H_2^{(i)}\right) \qquad e_k^{*v\,(i)} - e^{(i)} + e^{tr\,(i)} + h_k^{*(i)} = 0 \tag{54}$$

$$(H_3) \qquad d - \frac{L}{K^{tr2}} \|\boldsymbol{e} - \boldsymbol{e}^{tr}\|^2 - \sum_{k=1}^{M} \frac{L_k^*}{K_k^{*tr2}} \|\boldsymbol{e} - \boldsymbol{e}_k^{*v} - \boldsymbol{e}^{tr}\|^2 = 0 \tag{55}$$

$$\left(H_4^{(i)}\right) \qquad b^{(i)} - G_0^{*tr}(e^{(i)} - e_n^{tr\,(i)}) + h e_n^{tr\,(i)} + \frac{\tau_M + d}{x} e_n^{tr\,(i)} + 2\sum_{k=1}^{M} G_k^{*tr} e_k^{*v\,(i)} = 0 \tag{56}$$

$$\left(H_5^{(i)}\right) \qquad e^{tr\,(i)} - \frac{G_0^{*tr} e^{(i)} - \sum 2G_k^{*tr} e_k^{*v\,(i)} - R_y \frac{b^{(i)}}{\|\boldsymbol{b}\|}}{(G_0^{*tr} + h + (\tau_M + d)/x)} = 0 \tag{57}$$

where $x = \|\boldsymbol{e}^{tr}\|$, and $(\bullet)^{(i)}$ are the eigenvalues of the tensor $(\bullet)$.

Monodomain. In the monodomain phase, the system formed by equations (58)-(62) must be solved to find γ, $\boldsymbol{e}^{tr}$ and $\boldsymbol{e}_k^{*v}$.

$$\left(H_1^{(i)}\right) \qquad e_k^{*v\,(i)} - e^{(i)} + e^{tr\,(i)} + h_k^{*(i)} = 0 \tag{58}$$

$$(H_2') \qquad d' - \frac{L}{G_p^2 \varepsilon_L^2}\|\boldsymbol{e} - \boldsymbol{e}^{tr}\|^2 + \sum_{k=1}^{M} \frac{L_k^*}{G_{kp}^{*2}\varepsilon_L^2}\|\boldsymbol{e} - \boldsymbol{e}_k^{*v} - \boldsymbol{e}^{tr}\|^2 = 0 \tag{59}$$

$$\left(H_3'^{(i)}\right) \qquad b'^{\,(i)} - G_{0m}^*(e^{(i)} - e_n^{tr\,(i)}) + h e_n^{tr\,(i)} + \frac{\tau_M + d' + \gamma}{\varepsilon_L} e_n^{tr\,(i)} + 2\sum_{k=1}^{M} G_{km}^* e_k^{*v\,(i)} = 0 \tag{60}$$

$$\left(H_4'^{(i)}\right) \qquad e^{tr\,(i)} - \frac{G_{0m}^* e^{(i)} - 2\sum G_{km}^* e_k^{*v\,(i)} - R_y \frac{b'^{\,(i)}}{\|\boldsymbol{b}'\|}}{G_{0m}^* + h + (\tau_M + \gamma + d')/\varepsilon_L} = 0 \tag{61}$$

$$(H_5') \qquad \gamma - \left\| G_{0m}^* \boldsymbol{e} - \sum_{k=1}^{M} 2G_{km}^* \boldsymbol{e}_k^{*v} - R_y \frac{\boldsymbol{b}'}{\|\boldsymbol{b}'\|} \right\| + \tau_M + d' + (G_{0m}^* + h)\varepsilon_L = 0 \tag{62}$$

We will solve this system with a Newton-Raphson algorithm (derivations are detailed in Appendix A).

2.4. Coupling considerations

To investigate the influence of the coupling between the soft elasticity due to mesogen rotation and the viscoelasticity of the polymer chains, we compare three combinations of viscoelastic elements: decoupled, coupled, and full. In the decoupled model, all viscoelastic elements are decoupled from the soft elastic slider (Fig. 2, $M = 0$). In the coupled model, they are all coupled to the soft elasticity (Fig. 2, $N = 0$). The full model allows for some elements to remain decoupled while others will be coupled to the soft elasticity (Fig. 2, $M > 0$ and $N > 0$).

2.4.1. Decoupled model

In the decoupled model, we assume that the soft elasticity is completely elastic and all viscoelastic mechanisms are fully decoupled from this nonlinear elastic response. When $M = 0$, the deviatoric constitutive equations (11)-(12) simplify to

$$\boldsymbol{s} = 2G^{tr}\left(\boldsymbol{e} - \boldsymbol{e}^{tr}\right) + 2\sum_{k=1}^{N} G_k\left(\boldsymbol{e} - \boldsymbol{e}_k^{v}\right) \tag{63}$$

$$\boldsymbol{\chi} = 2G^{tr}\left(\boldsymbol{e} - \boldsymbol{e}^{tr}\right) - \left(\frac{L}{K^{tr\,2}}\|\boldsymbol{e} - \boldsymbol{e}^{tr}\|^2 + h\|\boldsymbol{e}^{tr}\| + \tau_M + \gamma\right)\partial\|\boldsymbol{e}^{tr}\| \tag{64}$$

2.4.2. Coupled model

In the coupled model, all the viscoelastic relaxations are coupled with the soft elastic slider. The mesogen rotation, measured by $\boldsymbol{e}^{tr}$, influences the response of the elastic and viscoelastic elements. When $N = 0$, the deviatoric constitutive equations (11)-(12) become

$$\boldsymbol{s} = 2G^{tr}\left(\boldsymbol{e} - \boldsymbol{e}^{tr}\right) + 2\sum_{k=1}^{M} G_k^*\left(\boldsymbol{e} - \boldsymbol{e}^{tr} - \boldsymbol{e}_k^{*v}\right) \tag{65}$$

$$\boldsymbol{\chi} = G_0^{*tr}\left(\boldsymbol{e} - \boldsymbol{e}^{tr}\right) - \left(d + h\|\boldsymbol{e}^{tr}\| + \tau_M + \gamma\right)\partial\|\boldsymbol{e}^{tr}\| - \sum_{k=1}^{M} 2G_k^{*tr}\boldsymbol{e}_k^{*v} \tag{66}$$

2.4.3. Full model

In the full model, we assume that M relaxation mechanisms are coupled to the mesogen rotation and soft elasticity, and their modulus evolves during the PM transition. The N decoupled viscoelastic elements are independent of soft elasticity and their modulus remains constant during the PM transition. The underlying assumption of the partially coupled model is that some polymer chain movements occur during mesogen rotation, while others are replaced by the rotation accommodating some of the imposed deformation.

2.5. Significance of the material parameters

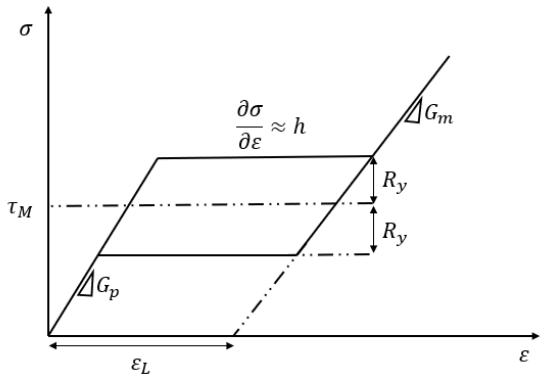

Figure 3: Schematic $\sigma - \epsilon$ diagram of the elastic part of the behavior under uniaxial loading

LCEs are assumed perfectly incompressible materials. Consequently, their Poisson's ratio is $\nu = 0.5$ and their bulk modulus κ is infinity.

The constitutive model has six material parameters for the deviatoric elastic part of the behavior (Fig. 3). The polydomain and monodomain shear moduli, G_p and G_m, control the slope of the stress-strain curve in the polydomain and monodomain regions. The threshold stress τ_M defines the stress at the onset of transition and soft elasticity, which is then supposed independent of strain rate. The strain ε_L controls the length of the transition region. More precisely, ε_L measures the residual strain at the end of the transition.

The parameters R_y and h define the hysteresis and hardening during the phase transition, respectively. These material parameters will first be set at $R_y = 0$ and $h = 0$ to indicate that the hysteresis during the transition may be well represented by the viscoelastic mechanisms already included in the model. Similarly, the soft elasticity is first assumed leading to a perfect plateau with a slope null.

The model also has $2 \times (M + N)$ material parameters for the deviatoric viscoelastic contribution to the mechanical behavior, *i.e.* the relaxation times τ_k and corresponding moduli G_k of M coupled and N decoupled viscoelastic elements.

The optimization is performed in MATLAB using the Levenberg-Marquart optimization algorithm. The optimization process involves multiple steps, with the first step focusing on defining the polydomain behavior, which encompasses all G_p and $G_k + G^*_{kp}$ quantities. Subsequent steps involve defining G_m, G^*_{km}, ϵ_L, and τ_M. Finally, all the obtained parameters are used as initial guesses, and the entire optimization is performed to determine the best distribution of relaxation mechanisms to coupled and decoupled parts, as well as the best fit for all parameters.

3. Results and Discussion

The aim of this paper is to (1) determine if the mesogen rotation is a relevant viscous mechanism, (2) investigate the coupling between mesogen rotation and the viscoelasticity of the polymer network, and (3) explore if the initiation of the mesogen rotation is a viscoelastic process. Before answering these questions, we will fit the model with different coupling considerations to the experimental data to compare the "best fit" behaviors.

3.1. Calibration of the model on experimental data

3.1.1. Experimental data

The model is calibrated using Dynamic Mechanical Analysis (DMA) and uniaxial tensile tests of a polydomain LCE. The data and its acquisition has been described in Azoug et al. [4].

For the DMA tests, a rectangular LCE specimen was subjected to a frequency sweep between 0.15 Hz and 40 Hz at 0.1 % strain amplitude. The test was repeated at several temperatures between $-20°$C and 80°C. The time-temperature superposition was used to obtain the master curve of the storage and loss moduli at the reference temperature of 20°. These tests will inform the distribution of relaxation times necessary for the model.

For the uniaxial tensile tests, a dumbbell LCE specimen was stretched from 0 to 100 % engineering strain at room temperature at multiple strain rates (from 0.005 $\%s^{-1}$ to 20 $\%s^{-1}$) and unloaded to zero force. These results indicate significant rate effects, where the onset, slope, and length of the soft elasticity plateau increase with strain rate. The model aims to accurately predict these effects.

3.1.2. Relaxation spectrum

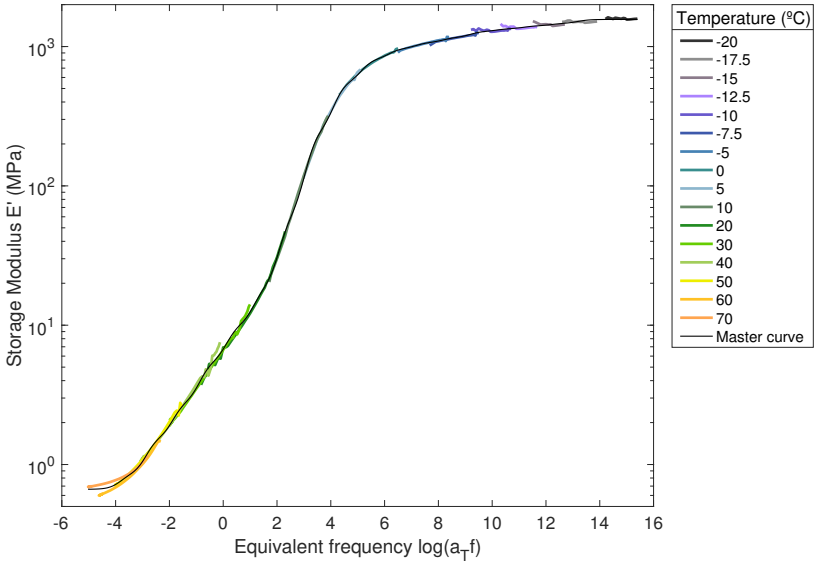

Figure 4: Master curve of the storage modulus at 20°C [4] and fit of a Generalized Maxwell model.

A generalized Maxwell model is fitted to the experimental master curve of the storage modulus to find the number of Maxwell elements required to accurately represent the relaxation spectrum (Fig. 4). The relaxation times τ_k are chosen as one per decade between 10^{-14} s and 10^3 s. The optimization determines the 18 viscoelastic moduli $\bar{E}_k$ corresponding to these relaxation times. The shear moduli $\bar{G}_k$ (Table 1) are deduced from $\bar{G}_k = \bar{E}_k/2(1+\nu)$ where $\nu = 0.5$ is the Poisson's ratio of the incompressible material. The elastic shear modulus, *i.e.* the modulus at infinite times, is identified as $\bar{G}_\infty = 0.35$ MPa.

Table 1: Discretized relaxation spectrum of the polydomain LCE.

k	1	2	3	4	5	6	7	8	9
$\log(\tau_k)$ (s)	3	2	1	0	-1	-2	-3	-4	-5
$\bar{G}_k$ (MPa)	0.062	0.24	0.41	0.89	1.53	2.74	13.85	63.24	104.18
k	10	11	12	13	14	15	16	17	18
$\log(\tau_k)$ (s)	-6	-7	-8	-9	-10	-11	-12	-13	-14
$\bar{G}_k$ (MPa)	85.34	50.95	33.81	30.25	41.43	19.22	21.66	18.95	33.06

3.1.3. Uniaxial tensile tests at multiple strain rates

In order to obtain the material parameters and the distribution of coupled and decoupled viscoelastic elements, the model is fitted to engineering stress-strain curves at strain rates between 0.005 $\%s^{-1}$-20 $\%s^{-1}$ (Fig. 5).

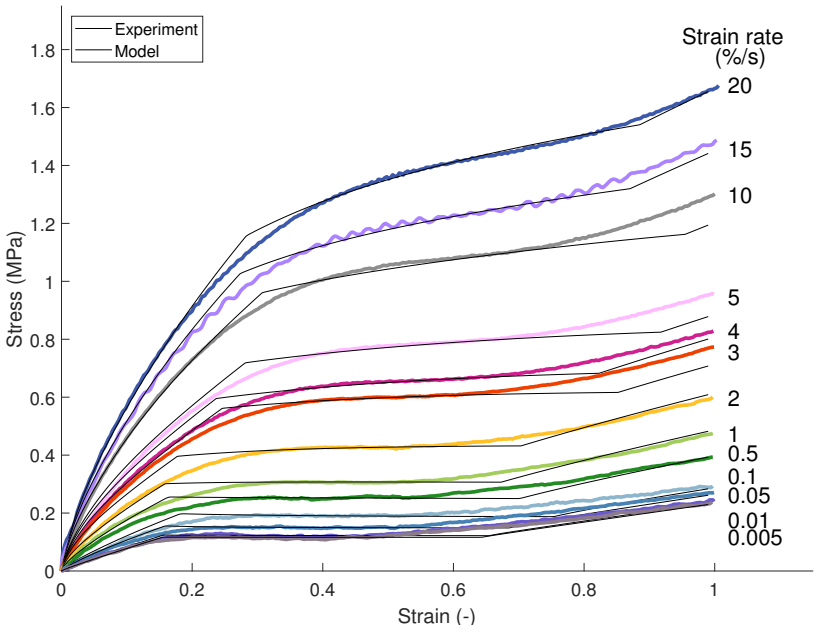

Figure 5: Fit of the full model to the experiments

At these strain rates, the relaxation mechanisms activated are the ones associated with the relaxation times τ_k = 1000, 100, 10, 1, 0.1, and 0.01 s, corresponding to elements k = 1 to 6. In the polydomain region, the values of the shear modulus G_p = 0.35 MPa and the six viscoelastic moduli G_{kp} = 0.062, 0.24, 0.41, 1.5, 2.7, and 2.74 MPa are obtained by least square fitting (Table 2). These values are identical to the moduli $\bar{G}_\infty$ and $\bar{G}_k$ (Table 1), except for the moduli associated with times 0.1 and 1 s, where the difference could be attributed to experimental errors during uniaxial testing at high strain rates. As the model differentiates between coupled and decoupled relaxation mechanisms, the optimization then imposes that the optimized total $G_{kp} = G_k + G^*_{kp}$ equals the sum of the decoupled and coupled polydomain moduli. The distribution of the viscoelasticity between coupled and decoupled elements shows that the relaxation mechanisms corresponding to long decoupled times and short coupled times are not necessary to correctly represent the behavior (Table 2).

In the monodomain region, the total viscoelastic moduli are $G_{km} = G_k + G^*_{km}$ = 0.03, 0.12, 0.35, 1.5, 2.7, and 2.74 MPa. The fitted monodomain elastic shear modulus is G_m = 0.16 MPa and the viscoelastic moduli for the coupled elements $k = 1-3$ become G^*_{km} = 0.03, 0.12, and 0.08 MPa (Table 2). This significant decrease during the transition does not correlate with the alignment of mesogens from polydomain to monodomain and is discussed in section 3.5.

Finally, the optimized parameters of the soft elasticity are ε_L = 0.35 and $\tau_M = 0.19 - 0.9$ MPa. The parameters h and R_y are set at 0 and 10^{-5} MPa (see discussion in Section 3.3). It was not possible to obtain a good correlation between the model and the experimental measurements with a constant value of τ_M. This will be discussed in detail in Section 3.4.

The model accurately predicts the modulus in the polydomain, PM transition, and monodomain regions according to strain rate, in the studied range of strain rates. Because of the distribution of relaxation mechanisms between coupled and decoupled contributions, the model is particularly efficient at determining the slope of the soft elastic region, which increases with strain rate and corresponds to the decoupled mechanisms only. The proper division of these six viscoelastic mechanisms into coupled and decoupled

Table 2: Material parameters of the coupled and decoupled Maxwell elements

	k	1	2	3	4	5	6
Times	τ_k (s)	1000	100	10	1	0.1	0.01
Decoupled	G_k (MPa)	-	-	0.27	1.5	2.7	2.74
Coupled	G^*_{kp} (MPa)	0.062	0.24	0.14	-	-	-
	G^*_{km} (MPa)	0.03	0.12	0.08	-	-	-
Total	G_{kp} (MPa)	0.062	0.24	0.41	1.5	2.7	2.74
	G_{km} (MPa)	0.03	0.12	0.35	1.5	2.7	2.74

elements ensures the ability of the model to predict the influence of strain rates in both the polydomain and soft elasticity regions of the stress-strain curve.

The strain range of the soft elastic region is overestimated in the model response at high strain rates. This correlates with stronger viscoelastic effects leading to the soft elasticity region exhibiting a positive tangent modulus and with a lack of experimental data in the monodomain region at high strain rates. At low strain rates, the soft elastic region ends between 40 and 60% engineering strain, and the modulus is measured in the monodomain state at higher strains. For high strain rates, the end of the soft elastic region is less obvious and occurs around 80%. The prediction of the strain range of the soft elasticity region is adequate at low and moderate strain rates, between 0.005 and 2%.s^{-1}.

The prediction of the modulus of the monodomain LCE remains challenging, partly because of the lack of clear experimental data in the monodomain region at high strain rates. The modulus in the monodomain region is mostly determined by the monodomain viscoelastic moduli G^*_{km}, as the moduli of the coupled elements evolve from a polydomain value to a monodomain value. These monodomain values are determined from the experiments as the value provided the closest fit and remain tentative.

3.2. Question (1) - What is the coupling between mesogen rotation and polymer chains viscoelasticity?

The decoupled, coupled, and full models, were fitted to experimental data (Fig. 6). Parameters were optimized to best fit the experimental curves at the strain rate of 5 %s^{-1}.

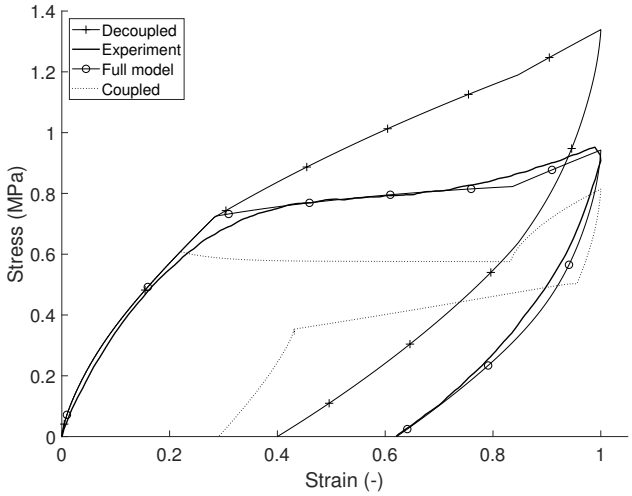

Figure 6: Decoupled, coupled, and full models compared with uniaxial tensile measurements at 5 %/s. For the full model, $G_p = 0.35$ Mpa, $G_m = 0.16$ Mpa, $\tau_M = 0.9$ Mpa, $\varepsilon_L = 0.25$. For the coupled and decoupled model, the viscoelastic moduli are identical to the moduli of the full model, $\tau_M = 0.9$ Mpa, $\varepsilon_L = 0.36$ and $\tau_M = 0.42$ Mpa, $\varepsilon_L = 0.28$, respectively.

In the polydomain region, $\boldsymbol{e}^{tr} = 0$, all models predict the same stress response, which closely follows the

experimental measurement. The main challenge remains to predict the effective modulus during the PM transition for all strain rates as well as the hysteresis.

By definition, all viscoelastic relaxation mechanisms of the coupled model are inactive during the transition, leading to almost perfect soft elasticity, meaning very low modulus. The slope is not perfectly zero in the coupled model because the change of modulus from polydomain to monodomain value leads to a small effective modulus and hysteresis. We measured an increase in slope with strain rate, which indicates that viscoelastic mechanisms are active during the transition. Consequently, this model is not capable of predicting the large change in slope and hysteresis observed with increasing strain rates.

For the decoupled model, the modulus during the transition is significantly higher than the one measured. The elastic part of the model is similar to the one in the coupled and full models and exhibits a perfect soft elasticity. However, in the decoupled model, all viscoelastic relaxation mechanisms remain active during the transition, and the large viscoelastic effects dominate the material response. Consequently, the decoupled model cannot properly predict both the softening phenomenon during the transition and the viscoelasticity of the polydomain and monodomain phases. We conclude that some viscoelastic relaxation mechanisms are necessarily inactive during the transition.

The viscoelastic response of the full model is the sum of the coupled and decoupled viscoelastic mechanisms contributions. The coupled mechanisms include evolving moduli between polydomain and monodomain phases while the decoupled moduli are constant. The responses in the polydomain and monodomain regions are similar to decoupled and coupled models. However, the stress prediction in the transition region is fitting the experimental data very well, in terms of onset, transition modulus, and end of the transition region. Since the N decoupled viscoelastic elements are independent of the transition, they dissipate energy in the polydomain, monodomain, and transition region. The shear moduli of the decoupled viscoelastic elements control the slope of the transition region. So contrary to the decoupled model where all relaxation mechanisms would remain active during the transition and to the coupled model where no relaxation mechanisms would be active during the transition, the full model allows for a few relaxation mechanisms to remain active during the transition while the others are inactive. This partial coupling leads to better control of the behavior of the LCE during the transition, but also of the effective onset and end of the transition region.

In conclusion, these results show that the coupling cannot be ignored, although it is not total. The remaining question is which relaxation mechanisms should be coupled or decoupled to best represent the observed mechanical behavior. Several relaxation mechanisms are associated with the movements of the polymer network. Schematically, long-time relaxation mechanisms are associated with slow movements of a large portion of the polymer chain, while short-time relaxation mechanisms are attributed to the movement of smaller polymer segments. Interestingly, optimal material parameters distribute the relaxation mechanisms as short-time decoupled (0.01 s - 10 s) and long-time coupled (10s - 1000 s), with an overlap for the relaxation time of 10 s.

This indicates that the long-range movements stop during the PM transition. The displacement imposed to the network is accommodated by the rotation of the elongated mesogens in the direction of the applied strain. Long-range rearrangements of polymer chains are not necessary during that phase.

As the mesogens are attached to the polymer backbone, mesogen rotation does imply some movements of the polymer segments in the direct vicinity of the mesogens, similar to the smaller movements occurring during classic polymer network deformation. So, short-time relaxation mechanisms occur throughout the deformation of the material, from polydomain, to PM transition, to monodomain, and are decoupled from the sliding device.

3.3. Question (2) - Is the mesogen rotation a viscous mechanism?

The comparison of the models with experimental data (Fig. 6) brings some answers to our second question: *Is mesogen rotation viscous?*. We are able to faithfully predict the stress response of the LCE across all the strain rates without including a mesogen viscoelastic or viscous mechanism and with parameters h and R_y essentially zero. R_y defines the hysteresis around the phase transition, introducing dissipation in the reversible sliding device, and h the hardening as the device is sliding, thus providing a slope to the response during the transition. Both these parameters are kept at zero for all models, indicating that those effects are not needed to accurately represent the behavior of LCEs.

A mesogen rotation viscoelastic mechanism would provide a time-dependent dissipation associated with mesogen rotation, as recently introduced in [52]. This is represented by a dashpot parallel to the sliding device. The introduction of this element would be physically relevant and accurate. However, the relaxation time associated with such a mechanism would necessarily remain small, on the order of 10^{-2} s [18, 48]. This would not have a significant impact on the stress response studied here. In addition, the mesogens are attached to a polymer chain network in LCEs, and the viscosity of the polymer chains dominates the mechanical response. This leads to a large restoring torque exerted by the network on mesogens and prevents an ideal soft elasticity [35]. The role of restoring torque and resistance of the network to mesogen rotation is already included in the proposed model as decoupled viscoelastic mechanisms.

To conclude, although the viscosity of mesogen rotation is physically accurate, its influence is not significant on the viscoelastic response of the LCE. As a result, we model the mesogen rotation as an elastic phenomenon and suppose that no significant amount of energy is dissipated through the movement of the mesogens. However, the polymer chains can move during the PM transition and dissipate energy, which the decoupled mechanisms represent. This conclusion concerns mainly the slope of the transition region. The initiation of the transition is discussed in the next section.

3.4. Question (3) - Is the initiation of mesogen rotation viscous?

In the proposed rheological model, we assume that τ_M is an elastic parameter representing the critical stress under equilibrium conditions. However, for the model to properly predict the measured experimental response, we had to consider the parameter τ_M varying with strain rate: τ_M increases from 0.19 to 0.9 with strain rates from $0.005\%s^{-1}$ to $20\%s^{-1}$ (Fig. 7). The effect of the strain rate is much more pronounced at strain rates above $1\%s^{-1}$ than at lower strain rates.

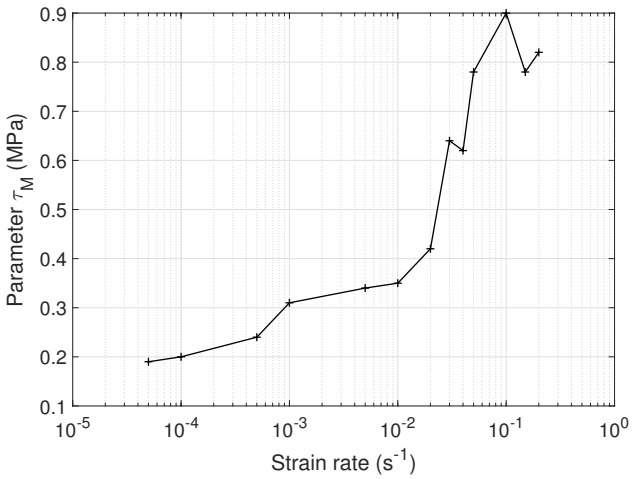

Figure 7: Rate-dependent threshold stress τ_M fitting the experimental data.

The stress at which the PM transition and the soft elasticity occur has been studied both numerically [41, 61] and experimentally [34, 21]. This threshold stress results from the presence of defects, which, in LCEs, are the crosslinks themselves. To better understand the microstructural origin of this threshold, Fridrikh and Terentjev [14] proposed a one-dimensional theoretical study of the threshold stress in an LCE at equilibrium in small strains. They developed a free energy with terms corresponding to the deformation of the wall between domains A and B separated by a wall of width w and to the mismatched deformation of the two neighboring domains when the domain A deforms softly, with no energy cost (Fig. 8a). Each domain is oriented with a director n, perpendicular to each other. The dimensions of the domain A are l for the initial configuration and $l_{||}$ and $l_{\perp}$ for the deformed configuration. The obtained threshold stress σ_t is proportional to the modulus μ and the domain anisotropy $r = l_{||}/l_{\perp}$ (equ. (67)).

$$\sigma_t = \mu(r-1) \tag{67}$$

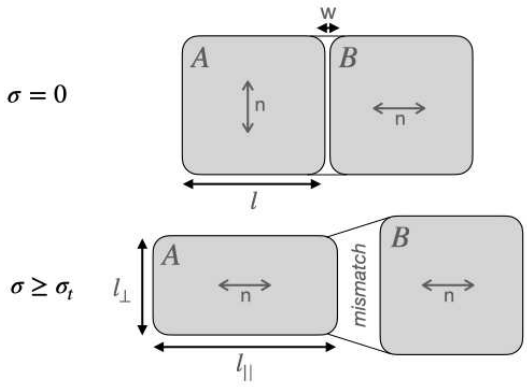

(a) Representation of the deformation mismatch between domains (inspired by [14]).

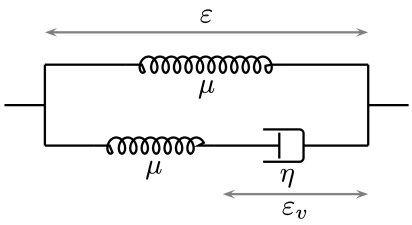

(b) Rheological model of the LCE behavior in domains A and B

Figure 8: Theoretical study of the threshold stress for the PM transition

Following the same reasoning, we introduce viscoelastic effects into the mismatched deformation of the two neighboring domains. The LCE viscoelastic behavior is represented by a Zener model (Fig. 8b), where the elastic and viscoelastic shear moduli are equal to μ and ε_v is the strain in the viscous dashpot. We obtain the following expression for the mechanical free energy per unit volume Ψ of the polydomain LCE under uniaxial elongation:

$$\Psi = \frac{\mu}{2}\left(\varepsilon^2 + (\varepsilon - \varepsilon_v)^2\right) + \frac{\mu}{2}\frac{w}{l}\left(\varepsilon^2 + (\varepsilon - \varepsilon_v)^2\right) + \frac{\mu}{2}\frac{l}{w}(r-1)^2 \tag{68}$$

The first term represents the free energy associated with the deformation of domain B, the second the free energy of the deformation of the wall, and the third the energy of the mismatch between the two domains at the domain wall. The equilibrium domain wall width is then $w^* = [l(r-1)]/(\varepsilon^2 + (\varepsilon - \varepsilon_v)^2)^{1/2}$, and the threshold stress becomes

$$\sigma_t = \frac{\mu(r-1)(2\varepsilon - \varepsilon_v)}{(\varepsilon^2 + (\varepsilon - \varepsilon_v)^2)^{1/2}} \tag{69}$$

If $\varepsilon_v = 0$, the threshold stress σ_t is a constant, as established by Fridrikh and Terentjev [14]. But otherwise, σ_t depends on the amount of viscous strains in the system.

Hence, this simple one-dimensional theoretical study indicates that the threshold stress should be strain rate dependent. Although the proposed model includes the influence of the viscoelastic elements on the threshold, in addition to τ_M representing a threshold intrinsic to the mesogen rotation (equ. (31)), this is not sufficient to reproduce the time-dependency of the behavior. Additional viscous mechanisms directly related to mesogen rotation should be integrated to the model. This will be the subject of further studies.

3.5. Limitations

This work focused on how the coupling between soft elasticity and viscoelasticity can be integrated to constitutive equations in a tractable model. We showed that dividing viscoelastic mechanisms into coupled long time mechanisms and decoupled short time mechanisms can properly describe the viscoelastic soft elasticity behavior of LCEs. However, the Helmholtz free energy function and the constitutive equations were developed in the framework of small deformation. This is not a good assumption for incompressible materials at high elongation and it has notably proven limited in the monodomain region, past the PM transition. In future work, we will extend the model to the framework of finite strain.

The obtained elastic and viscoelastic moduli in the polydomain phase are higher than the ones in the monodomain phase, contrasting with previous literature and with expectations from the physics of the material. Logically, the oriented monodomain has a higher modulus in the director's direction than the

polydomain that does not exhibit a preferred direction. In the case of incompressible materials under uniaxial tension and at a 100% deformation level, the cross-sectional area significantly decreases. The engineering stress σ is determined from the initial cross-sectional area A_0, while the true stress is determined from the current cross-sectional area A. Assuming LCEs remain perfectly incompressible, we determine the true stress-strain curve from the current cross-sectional area (Fig. 9). At large strains, A significantly differs from A_0, leading to large differences between engineering and true stress-strain curves. Fitting the model to the engineering and true stress-strain curves at a low strain rate of 0.005%/s leads to $G_p = 0.35$ MPa and $G_m = 0.16$ MPa, and $G_p = 0.4$ MPa and $G_m = 0.55$ MPa, respectively. This small-strain model is unable to capture the non-linear behavior at higher strains. Thus, we opted to fit the model to the engineering stress-strain curve, where the significant change in cross-sectional area is disregarded. The determination of physically meaningful monodomain parameters will be contingent upon the development of the finite strain model.

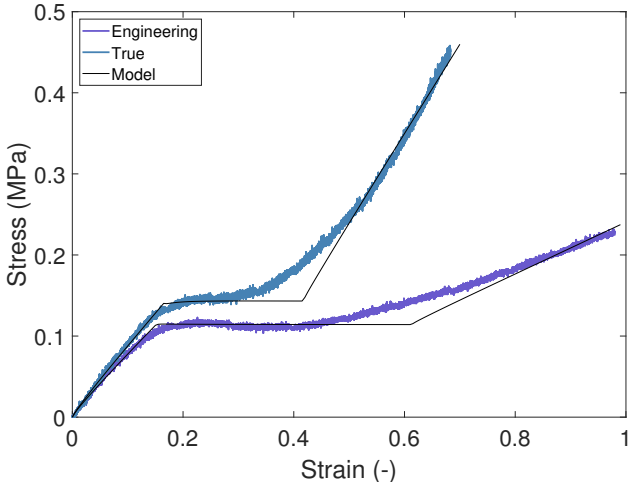

Figure 9: Responses of the model fitted to engineering and true stress-strain behavior at 0.005 %/s. The obtained parameters are $G_p = 0.35$ MPa and $G_m = 0.16$ MPa for the engineering stress, $G_p = 0.4$ MPa and $G_m = 0.55$ MPa for the true stress.

Finally, similarly to [52], the model does not incorporate the change in material anisotropy due to the transition. The polydomain LCE is macroscopically isotropic, while the monodomain LCE is strongly anisotropic. This aspect will need to be added in the future to properly represent the response to any loading in the nematic temperature domain.

These limitations have little impact on the current paper, which focuses on investigating the viscoelastic behavior during the PM transition more than at predicting absolute values of stresses and strains in the oriented high strain region.

4. Conclusion

In this paper, we addressed several key questions related to the soft elastic viscoelastic behavior of LCEs by developing a constitutive model and comparing it with experimental data. Our investigation aimed to explore the coupling between mesogen rotation and the polymer network's viscoelasticity, determine the relevance of mesogen rotation as a viscous mechanism, and investigate whether the initiation of mesogen rotation can be considered a viscoelastic process.

The small strain relaxation spectrum was captured by a generalized Maxwell model fitted to a master curve of the storage modulus. Uniaxial tensile tests at various strain rates provided insights into the influence of strain rate on the PM transition behavior. Coupled and decoupled models were incapable of predicting the time-dependent response, indicating that a combination of coupled and decoupled relaxation mechanisms is necessary. By considering coupled and decoupled relaxation mechanisms, the full model properly captured the behavior of LCEs in the polydomain, PM transition, and monodomain regions.

We improved the understanding of the time-dependent mechanical response of LCEs during the PM transition. Notably, the long relaxation mechanisms ($\tau \geq 10$ s) are coupled, while the short relaxation mechanisms ($\tau \leq 10$ s) are decoupled. Furthermore, the initiation of mesogen rotation is strain rate dependent, indicating some impact of the viscous strain on the threshold stress generally considered for the initiation of soft elasticity. This finding enriches our understanding of the underlying mechanisms driving the PM transition.

Future work will include extending the model to finite strain and compressive loading as well as investigating a proper modeling strategy for the initiation of mesogen rotation.

Acknowledgements

AA would like to thank the Oklahoma Center for the Advancement of Science & Technology (HR20-086) and the National Science Foundation CAREER program (CMMI 2238035) for their support.

Appendix A. Derivation details

To determine the internal variables during the PM transition and in the monodomain region, a system of equations must be solved numerically. Here we provide the derivations for the Newton-Raphson method.

PM transition. During the PM transition, the system of equations (A.1) -(A.5) must be solved:

$$H_1(x, \boldsymbol{e}^{tr}) = x - \|\boldsymbol{e}^{tr}\| \tag{A.1}$$

$$H_2^{(i)}(\boldsymbol{e}_k^{*v}, \boldsymbol{e}^{tr}) = e_k^{*v\,(i)} - e^{(i)} + e^{tr\,(i)} + h_k^{*(i)} = 0 \tag{A.2}$$

$$H_3(x, \boldsymbol{e}_k^{*v}, d, \boldsymbol{e}^{tr}) = d - \frac{L}{K^{tr\,2}}\|\boldsymbol{e} - \boldsymbol{e}^{tr}\|^2 - \sum_{k=1}^{M} \frac{L_k^*}{K_k^{*tr\,2}}\|\boldsymbol{e} - \boldsymbol{e}_k^{*v} - \boldsymbol{e}^{tr}\|^2 = 0 \tag{A.3}$$

$$H_4^{(i)}(x, \boldsymbol{e}_k^{*v}, d, \boldsymbol{b}, \boldsymbol{e}^{tr}) = b^{(i)} - G_0^{*tr}(e^{(i)} - e_n^{tr\,(i)}) + h e_n^{tr\,(i)} + \frac{\tau_M + d}{x} e_n^{tr\,(i)} + 2\sum_{k=1}^{M} G_k^{*tr} e_k^{*v\,(i)} = 0 \tag{A.4}$$

$$H_5^{(i)}(x, \boldsymbol{e}_k^{*v}, d, \boldsymbol{b}, \boldsymbol{e}^{tr}) = e^{tr\,(i)} - \frac{G_0^{*tr} e^{(i)} - \sum_{k=1}^{M} 2G_k^{*tr} e_k^{*v\,(i)} - R_y \frac{b^{(i)}}{\|\boldsymbol{b}\|}}{G_0^{*tr} + h + (\tau_M + d)/x} = 0 \tag{A.5}$$

The derivatives of H_1, $\boldsymbol{H}_2$, H_3, $\boldsymbol{H}_4$, and $\boldsymbol{H}_5$ with respect to x, $\boldsymbol{e}_k^{*v}$, d, b, and $\boldsymbol{e}^{tr}$ are obtained.

$$\frac{\partial H_1}{\partial x} = 1, \quad \frac{\partial H_1}{\partial e_k^{*v\,(j)}} = 0, \quad \frac{\partial H_1}{\partial d} = 0, \quad \frac{\partial H_1}{\partial b^{(j)}} = 0, \quad \frac{\partial H_1}{\partial e^{tr\,(j)}} = -\frac{e^{tr\,(j)}}{x}\ ,\ j = 1, 2, 3$$

$$\frac{\partial H_2^{(i)}}{\partial x} = 0, \quad \frac{\partial H_2^{(i)}}{\partial e_k^{*v\,(j)}} = \delta_{ij}, \quad \frac{\partial H_2^{(i)}}{\partial d} = 0, \quad \frac{\partial H_2^{(i)}}{\partial b^{(j)}} = 0, \quad \frac{\partial H_2^{(i)}}{\partial e^{tr\,(j)}} = \delta_{ij}\left(1 - e^{-(\Delta t_{n+1})/2\tau_k^*}\right)$$

$$\frac{\partial H_3}{\partial x} = \frac{2L(G_p - G_m)}{K^{tr\,3}}\|\boldsymbol{e} - \boldsymbol{e}^{tr}\|^2 + 2\sum_{k=1}^{M} \frac{L_k^*(G_{kp}^* - G_{km}^*)}{K_k^{*tr\,3}}\|\boldsymbol{e} - \boldsymbol{e}_k^{*v} - \boldsymbol{e}^{tr}\|^2$$

$$\frac{\partial H_3}{\partial e_k^{*v\,(j)}} = \frac{2L_k^*}{K_k^{*tr\,2}}(\boldsymbol{e}^{(j)} - \boldsymbol{e}_k^{*v\,(j)} - \boldsymbol{e}^{tr\,(j)}), \quad \frac{\partial H_3}{\partial d} = 1, \quad \frac{\partial H_3}{\partial b^{(j)}} = 0$$

$$\frac{\partial H_3}{\partial e^{tr\,(j)}} = \frac{2L}{K^{tr\,2}}(\boldsymbol{e}^{(j)} - \boldsymbol{e}^{tr\,(j)}) + 2\sum_{k=1}^{M} \frac{L_k^*}{K_k^{*tr\,2}}(\boldsymbol{e}^{(j)} - \boldsymbol{e}_k^{*v\,(j)} - \boldsymbol{e}^{tr\,(j)})$$

$$
\begin{aligned}
\frac{\partial H_4^{(i)}}{\partial x} &= -2\left(\frac{L}{K^{tr\,2}}+\sum_{k=1}^{M}\frac{L_k^*}{K_k^{*tr\,2}}\right)\left(\boldsymbol{e}^{(i)}-\boldsymbol{e}_n^{tr\,(i)}\right)\frac{\boldsymbol{e}^{tr}}{\|\boldsymbol{e}^{tr}\|}-\frac{\tau_M+d}{x^2}e_n^{tr\,(i)}+2\sum_{k=1}^{M}\frac{L_k^*}{K_k^{*tr\,2}}e_k^{*v\,(i)}\\
\frac{\partial H_4^{(i)}}{\partial e_k^{*v\,(j)}} &= 2G_k^{*tr}\delta_{ij},\quad \frac{\partial H_4^{(i)}}{\partial d}=\frac{e_n^{tr\,(i)}}{x},\quad \frac{\partial H_4^{(i)}}{\partial b^{(j)}}=\delta_{ij},\quad \frac{\partial H_4^{(i)}}{\partial e^{tr\,(j)}}=0\\
\frac{\partial H_5^{(i)}}{\partial x} &= \frac{2}{(G_0^{*tr}+h+(\tau_M+d)/x)}\left[\sum_{k=1}^{M}\frac{L_k^*}{K_k^{*tr\,2}}e_k^{*v\,(i)}-\left(\frac{L}{K^{tr\,2}}+\sum_{k=1}^{M}\frac{L_k^*}{K_k^{*tr\,2}}\right)e^{(i)}\right]\\
&\quad -\frac{\left(G_0^{*tr}e^{(i)}-2\sum_{k=1}^{M}G_k^{*tr}e_k^{*v\,(i)}-R_y\frac{b^{(i)}}{\|\boldsymbol{b}\|}\right)(\tau_M+d)}{\left((G_0^{*tr}+h)x+\tau_M+d\right)^2}
\end{aligned}
$$

$$
\begin{aligned}
\frac{\partial H_5^{(i)}}{\partial e_k^{*v\,(j)}} &= \frac{2G_k^{*tr}}{G_0^{*tr}+h+(\tau_M+d)/x}\delta_{ij},\quad \frac{\partial H_5^{(i)}}{\partial d}=\frac{G_0^{*tr}e^{(i)}-2\sum_{k=1}^{M}G_k^{*tr}e_k^{*v\,(i)}-R_y\frac{b^{(i)}}{\|\boldsymbol{b}\|}}{x\left(G_0^{*tr}+h+(\tau_M+d)/x\right)^2}\\
\frac{\partial H_5^{(i)}}{\partial b^{(j)}} &= \frac{R_y}{G_0^{*tr}+h+(d+\tau_M)/x}\frac{\|\boldsymbol{b}\|^2\delta_{ij}-b^{(i)}b^{(j)}}{\|\boldsymbol{b}\|^3},\quad \frac{\partial H_5^{(i)}}{\partial e_{tr\,(j)}}=\delta_{ij}
\end{aligned}
\tag{A.6}
$$

Monodomain. In the monodomain phase, equations (A.7)-(A.11) must be solved to find $\boldsymbol{e}_k^{*v}$, d', $\boldsymbol{b}$, γ, and $\boldsymbol{e}^{tr}$.

$$
H_1'^{(i)}(\boldsymbol{e}_k^{*v},d',\boldsymbol{e}^{tr}) = e_k^{*v\,(i)}-e^{(i)}+e^{tr\,(i)}+h_n^{(i)}(e^{tr\,(i)})=0 \tag{A.7}
$$

$$
H_2'(\boldsymbol{e}_k^{*v},d',\boldsymbol{e}^{tr}) = d'-\frac{L}{G_p^2\varepsilon_L^2}\|\boldsymbol{e}-\boldsymbol{e}^{tr}\|^2+\sum_{k=1}^{M}\frac{L_k^*}{G_{kp}^{*2}\varepsilon_L^2}\|\boldsymbol{e}-\boldsymbol{e}_k^{*v}-\boldsymbol{e}^{tr}\|^2=0 \tag{A.8}
$$

$$
H_3'^{(i)}(\boldsymbol{e}_k^{*v},d',\boldsymbol{b}',\gamma,\boldsymbol{e}^{tr}) = b'^{(i)}-G_{0m}^*(e^{(i)}-e_n^{tr\,(i)})+he_n^{tr\,(i)}+\frac{\tau_M+d'+\gamma}{\varepsilon_L}e_n^{tr\,(i)}+2\sum_{k=1}^{M}G_{km}^*e_k^{*v\,(i)}=0 \tag{A.9}
$$

$$
H_4'^{(i)}(\boldsymbol{e}_k^{*v},d',\boldsymbol{b}',\gamma,\boldsymbol{e}^{tr}) = e^{tr\,(i)}-\frac{G_{0m}^*e^{(i)}-2\sum_{k=1}^{M}G_{km}^*e_k^{*v\,(i)}-R_y\frac{b'^{(i)}}{\|\boldsymbol{b}'\|}}{G_{0m}^*+h+(\tau_M+\gamma+d')/\varepsilon_L}=0 \tag{A.10}
$$

$$
H_5'(\boldsymbol{e}_k^{*v},d',\boldsymbol{b}',\gamma,\boldsymbol{e}^{tr}) = \gamma-\left\|G_{0m}^*\boldsymbol{e}-\sum_{k=1}^{M}2G_{km}^*\boldsymbol{e}_k^{*v}-R_y\frac{\boldsymbol{b}'}{\|\boldsymbol{b}'\|}\right\|+\tau_M+d'+(G_{0m}^*+h)\varepsilon_L=0 \tag{A.11}
$$

The derivatives of $\boldsymbol{H}_1'$, H_2' and $\boldsymbol{H}_3'$, $\boldsymbol{H}_4'$, and H_5' with respect to $\boldsymbol{e}_k^{*v}$, d', $\boldsymbol{b}'$, γ, and $\boldsymbol{e}^{tr}$ are

$$
\begin{aligned}
\frac{\partial H_1'^{(i)}}{\partial e_k^{*v\,(j)}} &= \delta_{ij}, \quad \frac{\partial H_1'^{(i)}}{\partial d'} = 0, \quad \frac{\partial H_1'^{(i)}}{\partial b'^{(j)}} = 0, \quad \frac{\partial H_1'^{(i)}}{\partial \gamma} = 0, \quad \frac{\partial H_1'^{(i)}}{\partial e^{tr\,(j)}} = \delta_{ij}\left(1 - e^{-(\Delta t_{n+1})/2\tau_k^*}\right) \\
\frac{\partial H_2'}{\partial e_k^{*v\,(j)}} &= \frac{2L_k^*}{G_{kp}^{*\ 2}\varepsilon_L^2}(\boldsymbol{e}^{(i)} - \boldsymbol{e}_k^{*v\,(i)} - \boldsymbol{e}^{tr\,(i)}), \quad \frac{\partial H_2'}{\partial d'} = 1, \quad \frac{\partial H_2'}{\partial b'^{(j)}} = 0, \quad \frac{\partial H_2'}{\partial \gamma} = 0 \\
\frac{\partial H_2'}{\partial e^{tr\,(j)}} &= \frac{2L}{G_p^2\varepsilon_L^2}(\boldsymbol{e}^{(i)} - \boldsymbol{e}^{tr\,(i)}) + 2\sum_{k=1}^{M}\frac{L_k^*}{G_{kp}^{*\ 2}\varepsilon_L^2}\left(\boldsymbol{e}^{(i)} - \boldsymbol{e}_k^{*v\,(i)} - \boldsymbol{e}^{tr\,(i)}\right) \\
\frac{\partial H_3'^{(i)}}{\partial e_k^{*v\,(j)}} &= 2G_{km}^*\delta_{ij}, \quad \frac{\partial H_3'^{(i)}}{\partial d'} = \frac{e_n^{tr\,(i)}}{\varepsilon_L}, \quad \frac{\partial H_3'^{(i)}}{\partial b'^{j}} = \delta_{ij}, \quad \frac{\partial H_3'^{(i)}}{\partial \gamma} = \frac{e_n^{tr\,(i)}}{\varepsilon_L}, \quad \frac{\partial H_3'^{(i)}}{\partial e^{tr\,(j)}} = 0 \\
\frac{\partial H_4'^{(i)}}{\partial e_k^{*v\,(j)}} &= \frac{2G_{km}^*}{G_0^* + h + (\tau_M + d + \gamma)/\varepsilon_L}\delta_{ij}, \quad \frac{\partial H_4'^{(i)}}{\partial d'} = \frac{G_{0m}^* e^{(i)} - 2\sum_{k=1}^{M} G_{km}^* e_k^{*v\,(i)} - R_y\frac{b'^{(i)}}{\|\boldsymbol{b}'\|}}{\varepsilon_L\left(G_{0m}^* + h + (\tau_M + d + \gamma)/\varepsilon_L\right)^2} \\
\frac{\partial H_4'^{(i)}}{\partial b'^{(j)}} &= \frac{R_y}{G_{0m}^* + h + (d + \tau_M + \gamma)/\varepsilon_L}\frac{\|\boldsymbol{b}'\|^2\delta_{ij} - b'^{(i)}b'^{(j)}}{\|\boldsymbol{b}'\|^3}, \quad \frac{\partial H_4'^{(i)}}{\partial \gamma} = \frac{\partial H_4'^{(i)}}{\partial d'}, \quad \frac{\partial H_4'^{(i)}}{\partial e^{tr\,(j)}} = \delta_{ij} \\
\frac{\partial H_5'}{\partial e_k^{*v\,(j)}} &= 2G_{km}^*\frac{G_{0m}^* e^{(j)} - 2\sum_{k=1}^{M} G_{km}^* e_k^{*v\,(j)} - R_y\frac{b'^{(j)}}{\|\boldsymbol{b}'\|}}{\|G_{0m}^*\boldsymbol{e} - 2\sum_{k=1}^{M} G_{km}^* e_k^{*v} - R_y\frac{\boldsymbol{b}'}{\|\boldsymbol{b}'\|}\|}, \quad \frac{\partial H_5'}{\partial d'} = 1, \quad \frac{\partial H_5'}{\partial \gamma} = 1, \quad \frac{\partial H_5'}{\partial e^{tr\,(j)}} = 0 \\
\frac{\partial H_5'}{\partial b'^{(j)}} &= \frac{R_y}{\|\boldsymbol{b}'\|\|\boldsymbol{W}\|}\left(W^{(j)} - \frac{b'^{(j)}}{\|\boldsymbol{b}'\|^2}\sum_{i=1}^{3} W^{(i)}b'^{(i)}\right), \quad \boldsymbol{W} = G_{0m}^*\boldsymbol{e} - 2\sum_{k=1}^{M} G_{km}^*\boldsymbol{e}_k^{*v} - R_y\frac{\boldsymbol{b}'}{\|\boldsymbol{b}'\|}\|
\end{aligned}
\tag{A.12}
$$

References

[1] Agra-Kooijman, D.M., Fisch, M.R., Joshi, L., Ren, W., McMullan, P.J., Griffin, A.C., Kumar, S., 2015. Dual relaxation and structural changes under uniaxial strain in main-chain smectic-c liquid crystal elastomer. Physical Chemistry Chemical Physics 17, 191–199.

[2] Auricchio, F., Reali, A., Stefanelli, U., 2009. A macroscopic 1D model for shape memory alloys including asymmetric behaviors and transformation-dependent elastic properties. Computer Methods in Applied Mechanics and Engineering 198, 1631–1637.

[3] Auricchio, F., Sacco, E., 1997. A one-dimensional model for superelastic shape-memory alloys with different elastic properties between austenite and martensite. International Journal of Non-Linear Mechanics 32, 1101–1114.

[4] Azoug, A., Vasconcellos, V., Dooling, J., Saed, M., Yakacki, C., Nguyen, T., 2016. Viscoelasticity of the polydomain-monodomain transition in main-chain liquid crystal elastomers. Polymer 98, 165–171.

[5] Beck, A., 2017. First-order methods in optimization. SIAM.

[6] Bladon, P., Terentjev, E., Warner, M., 1994. Deformation–induced orientational transitions in liquid crystals elastomer. Journal de Physique II 4, 75–91.

[7] Brannum, M.T., Steele, A.M., Venetos, M.C., Korley, L.T.J., Wnek, G.E., White, T.J., 2019. Light Control with Liquid Crystalline Elastomers. Advanced Optical Materials 7, 1801683.

[8] Clarke, S.M., Terentjev, E.M., 1999. Slow stress relaxation in liquid crystal elastomers and gels. Faraday Discussions 112, 325–333.

[9] Conti, S., DeSimone, A., Dolzmann, G., 2002. Soft elastic response of stretched sheets of nematic elastomers: A numerical study. Journal of the Mechanics and Physics of Solids 50, 1431 1451.

[10] De Jeu, W.H., 2012. Liquid crystal elastomers: materials and applications. volume 250. Springer.

[11] De Luca, M., DeSimone, A., Petelin, A., Čopič, M., 2013. Sub-stripe pattern formation in liquid crystal elastomers: Experimental observations and numerical simulations. Journal of the Mechanics and Physics of Solids 61, 2161–2177.

[12] Dorfmann, A., Ogden, R.W., 2004. A constitutive model for the mullins effect with permanent set in particle-reinforced rubber. International Journal of Solids and Structures 41, 1855–1878.

[13] Eisenberg, M., Phillips, A., 1971. A theory of plasticity with non-coincident yield and loading surfaces. Acta Mechanica 11, 247–260.

[14] Fridrikh, S., Terentjev, E., 1999. Polydomain-monodomain transition in nematic elastomers. Physical Review E 60, 1847.

[15] Gallani, J., Hilliou, L., Martinoty, P., Doublet, F., Mauzac, M., 1996. Mechanical behavior of side-chain liquid crystalline networks. Journal de Physique II 6, 443–452.

[16] Gallani, J., Hilliou, L., Martinoty, P., Keller, P., 1994. Abnormal viscoelastic behavior of side-chain liquid-crystal polymers. Physical review letters 72, 2109.
[17] Giamberini, M., Ambrogi, V., Cerruti, P., Carfagna, C., 2006-06. Viscoelasticity of main chain liquid crystalline elastomers. Polymer 47, 4490–4496.
[18] Hotta, A., Terentjev, E., 2001. Long-time stress relaxation in polyacrylate nematic liquid crystalline elastomers. Journal of Physics: Condensed Matter 13, 11453.
[19] Ikeda, T., Mamiya, J.i., Yu, Y., 2007. Photomechanics of Liquid-Crystalline Elastomers and Other Polymers. Angewandte Chemie International Edition 46, 506–528.
[20] Ilnytskyi, J.M., Saphiannikova, M., Neher, D., Allen, M.P., 2012. Modelling elasticity and memory effects in liquid crystalline elastomers by molecular dynamics simulations. Soft Matter 8, 11123–11134.
[21] Krause, S., Zander, F., Bergmann, G., Brandt, H., Wertmer, H., Finkelmann, H., 2009. Nematic main-chain elastomers: Coupling and orientational behavior. Comptes Rendus Chimie 12, 85–104.
[22] Leslie, F.M., 1992. Continuum theory for nematic liquid crystals. Continuum Mechanics and Thermodynamics 4, 167–175.
[23] Lubliner, J., 1991. A simple model of generalized plasticity. International journal of solids and structures 28, 769–778.
[24] Lubliner, J., Auricchio, F., 1996. Generalized plasticity and shape-memory alloys. International Journal of Solids and Structures 33, 991–1003.
[25] Mihai, A., Goriely, A., 2020. A pseudo-anelastic model for stress softening in liquid crystal elastomers. Proceedings of the Royal Society A 476, 20200558.
[26] Mihai, L.A., Wang, H., Guilleminot, J., Goriely, A., 2021. Nematic liquid crystalline elastomers are aeolotropic materials. Proceedings of the Royal Society A: Mathematical, Physical and Engineering Sciences 477, 20210259.
[27] Oates, W., Wang, H., 2009. A new approach to modeling liquid crystal elastomers using phase field methods. Modelling and Simulation in Materials Science and Engineering 17, 064004.
[28] Ogden, R.W., Roxburgh, D.G., 1999. A pseudo–elastic model for the mullins effect in filled rubber. Proceedings of the Royal Society of London. Series A: Mathematical, Physical and Engineering Sciences 455, 2861–2877.
[29] Ortiz, C., K. Ober, C., Kramer, E., 1998. Stress relaxation of a main-chain, smectic, polydomain liquid crystalline elastomer. Polymer 39, 3713–3718.
[30] Osari, K., Koibuchi, H., 2017. Finsler geometry modeling and monte carlo study of 3D liquid crystal elastomer. Polymer 114, 355–369.
[31] Prathumrat, P., Sbarski, I., Hajizadeh, E., Nikzad, M., 2021. A comparative study of force fields for predicting shape memory properties of liquid crystalline elastomers using molecular dynamic simulations. Journal of Applied Physics 129, 155101.
[32] Prévôt, M.E., Ustunel, S., Hegmann, E., 2018. Liquid Crystal Elastomers—A Path to Biocompatible and Biodegradable 3D-LCE Scaffolds for Tissue Regeneration. Materials 11, 377.
[33] Scalet, G., Peigney, M., 2017. A robust and efficient radial return algorithm based on incremental energy minimization for the 3D souza-auricchio model for shape memory alloys. European Journal of Mechanics - A/Solids 61, 364–382.
[34] Schätzle, J., Kaufhold, W., Finkelmann, H., 1989. Nematic elastomers: The influence of external mechanical stress on the liquid-crystalline phase behavior. Die Makromolekulare Chemie 190, 3269–3284.
[35] Schönstein, M., Stille, W., Strobl, G., 2001. Effect of the network on the director fluctuations in a nematic side-group elastomer analysed by static and dynamic light scattering. The European Physical Journal E 5, 511–517.
[36] Shaha, R.K., Merkel, D.R., Anderson, M.P., Devereaux, E.J., Patel, R.R., Torbati, A.H., Willett, N., Yakacki, C.M., Frick, C.P., 2020. Biocompatible liquid-crystal elastomers mimic the intervertebral disc. Journal of the mechanical behavior of biomedical materials 107, 103757.
[37] Simo, J., 1985. On the computational significance of the intermediate configuration and hyperelastic relations in finite deformation elastoplasticity. Mech. Mat. 4, 439–451.
[38] Simo, J., Ortiz, M., 1985. A unified approach to finite deformation elastoplastic analysis based on the use of hyperelastic constitutive equations. Comput. Methods Appl. Mech. Engrg. 49, 221–245.
[39] Skačej, G., 2018. Sample preparation affects the nematic–isotropic transition in liquid crystal elastomers: insights from molecular simulation. Soft Matter 14, 1408–1416.
[40] Skačej, G., Zannoni, C., 2012. Molecular simulations elucidate electric field actuation in swollen liquid crystal elastomers. Proceedings of the National Academy of Sciences 109, 10193–10198.
[41] Skačej, G., Zannoni, C., 2014. Molecular Simulations Shed Light on Supersoft Elasticity in Polydomain Liquid Crystal Elastomers. Macromolecules 47, 8824–8832.
[42] Sonnet, A., Maffettone, P., Virga, E., 2004. Continuum theory for nematic liquid crystals with tensorial order. Journal of Non-Newtonian Fluid Mechanics 119, 51–59.
[43] Sonnet, A.M., Virga, E.G., 2012. Dissipative Ordered Fluids: Theories for Liquid Crystals. Springer US, Boston, MA.
[44] Souza, A.C., Mamiya, E.N., Zouain, N., 1998. Three-dimensional model for solids undergoing stress-induced phase transformations. European Journal of Mechanics-A/Solids 17, 789–806.
[45] Stephen, M.J., Straley, J.P., 1974. Physics of liquid crystals. Reviews of Modern Physics 46, 617.
[46] Sun, Q.P., Hwang, K.C., 1993. Micromechanics modelling for the constitutive behavior of polycrystalline shape memory alloys—II. Study of the individual phenomena. Journal of the Mechanics and Physics of Solids 41, 19–33.
[47] Tagashira, K., Takahashi, K.Z., Fukuda, J.i., Aoyagi, T., 2018. Development of coarse-grained liquid-crystal polymer model with efficient electrostatic interaction: Toward molecular dynamics simulations of electroactive materials. Materials 11, 83.
[48] Terentjev, E., Hotta, A., Clarke, S., Warner, M., 2003. Liquid crystalline elastomers: dynamics and relaxation of microstructure. Philosophical Transactions of the Royal Society of London. Series A: Mathematical, Physical and Engineering

Sciences 361, 653–664.
[49] Terentjev, E., Warner, M., 2001. Linear hydrodynamics and viscoelasticity of nematic elastomers. The European Physical Journal E 4, 343–353.
[50] Terentjev, E.M., 1999. Liquid-crystalline elastomers. Journal of Physics: Condensed Matter 11, R239.
[51] Urayama, K., Honda, S., Takigawa, T., 2006. Slow dynamics of shape recovery of disordered nematic elastomers. Physical Review E 74, 041709.
[52] Wang, Z., Chehade, A.E.H., Govindjee, S., Nguyen, T.D., 2022. A nonlinear viscoelasticity theory for nematic liquid crystal elastomers. Journal of the Mechanics and Physics of Solids 163, 104829.
[53] Ware, T.H., Biggins, J.S., Shick, A.F., Warner, M., White, T.J., 2016. Localized soft elasticity in liquid crystal elastomers. Nature Communications 7, 10781.
[54] Warner, M., Bladon, P., Terentjev, E., 1994. "soft elasticity"—deformation without resistance in liquid crystal elastomers. Journal de Physique II 4, 93–102.
[55] Warner, M., Gelling, K., Vilgis, T., 1988. Theory of nematic networks. The Journal of chemical physics 88, 4008–4013.
[56] Warner, M., Terentjev, E.M., 2003. Liquid Crystal Elastomers. OUP Oxford.
[57] Warner, M., Terentjev, E.M., 2007. Liquid crystal elastomers. volume 120. Oxford university press.
[58] Warner, M., Wang, X., 1991. Elasticity and phase behavior of nematic elastomers. Macromolecules 24, 4932–4941.
[59] Wayman, C.M., 1989. An introduction to martensite and shape memory, in: Engineering Aspects of Shape Memory Alloys. Butterworth-Heinemann. chapter 1, pp. 3–20.
[60] Whitmer, J.K., Roberts, T.F., Shekhar, R., Abbott, N.L., De Pablo, J.J., 2013. Modeling the polydomain-monodomain transition of liquid crystal elastomers. Physical Review E 87, 020502.
[61] Yasuoka, H., Takahashi, K.Z., Fukuda, J.i., Aoyagi, T., 2021. Molecular architecture dependence of mesogen rotation during uniaxial elongation of liquid crystal elastomers. Polymer 229, 123970.
[62] Yin, L., Han, L., Ge, F., Tong, X., Zhang, W., Soldera, A., Zhao, Y., 2020. A Novel Side-Chain Liquid Crystal Elastomer Exhibiting Anomalous Reversible Shape Change. Angewandte Chemie 132, 15241–15246.
[63] Zannoni, C., 2000. Computer simulation and molecular design of model liquid crystals, in: Chemistry at the Beginning of the Third Millennium. Springer, pp. 329–342.
[64] Zhang, Y., Xuan, C., Jiang, Y., Huo, Y., 2019. Continuum mechanical modeling of liquid crystal elastomers as dissipative ordered solids. Journal of the Mechanics and Physics of Solids 126, 285–303.
[65] Zhu, W., Shelley, M., Palffy-Muhoray, P., 2011. Modeling and simulation of liquid-crystal elastomers. Physical Review E 83, 051703.